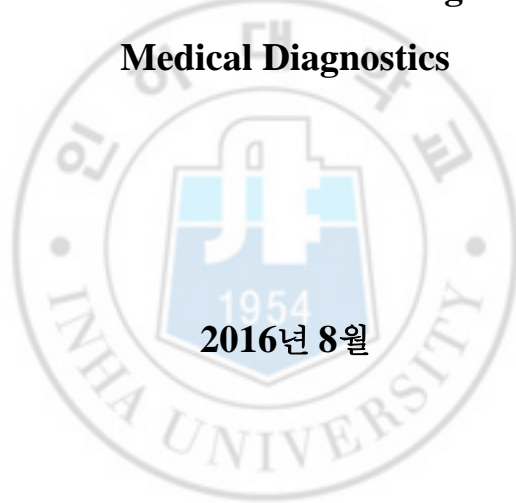# 질병진단 및 환경 모니터링을 위한 반도체식 산화물 그래핀 나노 복합체 가스 센서

Semiconducting Oxide-Graphene Nanocomposite Gas Sensors for Environmental Monitoring and Noninvasive Medical Diagnostics

2016년 8월
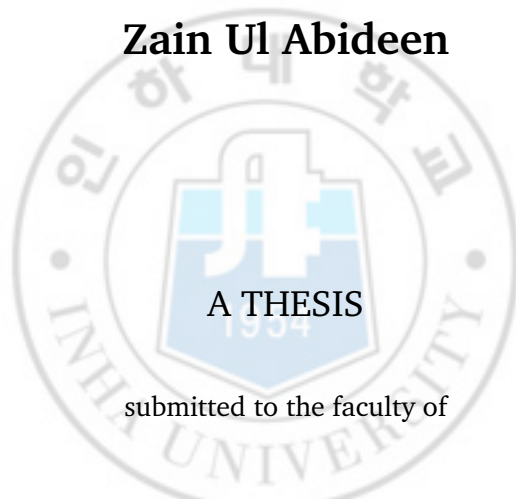
인하대학교 대학원

신소재공학과 (신소재공학전공)

자인울아비딘

Semiconducting Oxide-Graphene Nanocomposite Gas Sensors for Environmental Monitoring and Noninvasive Medical Diagnostics

By

Zain Ul Abideen

A THESIS

submitted to the faculty of

INHA UNIVERSITY

in partial fulfillment of the requirements

for the degree of

Master of Engineering

Department of Materials Science and Engineering

August 2016

Recommended Citation

Abideen, Z. U. (2016). *Semiconducting Oxide-Graphene Nanocomposite Gas Sensors for Environmental Monitoring and Noninvasive Medical Diagnostics* (Master's Thesis, Inha University, Republic of Korea).

이 논문을 자인울아비딘의 석사학위 논문으로 인정함

2016년 8 월

주심 _____ 정 대 용

부심 _____ 김 상 섭

위원 _____ 현 승 균

"I would like to dedicate my thesis to my Mom and Dad, who always

encouraged me to go on every adventure, especially this one... and for

teaching me to believe in myself...

and

To my Sisters"

AUTHOR'S DECLARATION

"I certify that except where due acknowledgement has been made, the work is that of the author alone; the work has not been submitted previously, in whole or in part, to qualify for any other academic award; the content of the thesis is the result of work which has been carried out since the official commencement date of the approved research program; and, any editorial work, paid or unpaid, carried out by a third party is acknowledged."

Zain Ul Abideen

ABSTRACT

In this thesis, the author developed and investigated nanostructured materials based chemoresistive devices for gas sensing applications. The synthesis of nanostructured materials, sensing device fabrication and their gas sensing performance have been carried out. The investigated materials are based on nanofibers, which are prepared by electrospinning process, and are uniformly distributed over silicon substrates in a web-like morphology. The n-type semiconductor materials, namely ZnO and SnO_2, are used as base materials and their sensitivity and selectivity have been significantly enhanced by using graphene-loaded SnO_2 and reduced graphene oxide-loaded ZnO composite nanofibers. The developed composite nanofibers based gas sensors have high surface to volume ratio and achieved very high sensitivity towards different gas species.

Sol-gel and electrospinning process were used to synthesize the composite nanofibers whereas magnetron sputtering was used to deposit metal layers on the composite nanofibers to make electrodes. Pd and Pt metal layers were deposited, on all the composite nanofibers synthesized by the author, to fabricate sensing devices. Various nanostructural characterizations were employed to extract information of composite nanofibers such as their structural morphology, interaction of second phase material (graphene or reduced graphene oxide) with the metal oxide (SnO_2 or ZnO), orientation and the nature of the second phase and the surface topology of the composite nanofibers. This information was required to understand the electrical properties of the composite nanomaterials and link its properties to their gas sensing characteristics.

Nanostructural characterization techniques such as scanning electron microscopy (SEM), transmission electron microscopy (TEM), X-ray diffraction (XRD) revealed that the developed composite nanofibers have polycrystalline,

one-dimensional nanostructure. It was also revealed that the composite nanofibers were comprised of large number of nanograins, which evolved during calcination, graphene or reduced graphene oxide nanosheets were present randomly like tiny islands in the nanofibers, and these *p*-type graphene or reduced graphene oxide nanosheets create localized *p-n* heterojunctions with the *n*-type semiconductors.

The gas sensing results reveal that the overall sensitivity of the composite nanofibers is greatly enhanced as compared to conventional materials and that the reduced graphene oxide-loaded ZnO composite nanofibers are extremely sensitive and selective towards H_2 gas while graphene-loaded SnO_2 based sensors are more sensitive and selective towards H_2S gas. However, all sensors showed excellent sensitivity towards various gas species and were tested at various temperatures. The temperature and the concentration of the second phase are optimized with respect to the base semiconductor material. In the case of reduced graphene oxide-loaded ZnO composite nanofibers, the optimized amount of reduced graphene oxide was found to be 0.44 wt% while the optimal amount of graphene in graphene-loaded SnO_2 composite nanofibers was 0.5 wt%. Graphene loading into SnO_2 nanofibers not only increased the sensitivity but also decreased the optimal operating temperature of the sensors as compared to pristine SnO_2 nanofibers. In addition, the camparison of the gas sensing characteristics of reduced graphene oxide-loaded ZnO and graphene-loaded SnO_2 composite nanofibers was also carried out. Finally, novel hybrid sensing mechanisms have been proposed as the possible reasons for extraordinary enhancement of sensitivity and selectivity of these composite nanofibers.

The author's investigations reveal that the graphitic carbon/metal oxide composite nanofibers based sensors produce higher sensitivity than metal oxide/metal oxide composite nanofibers.

ACKNOWLEDGEMENTS

During the 2 years' journey of my stay and research work in South Korea, there are many people, who supported and encouraged me to reach here and who are the reason of the successful completion of this journey. Furthermore, there are people who made this journey enjoyable and memorable. Although, words are very small to express my gratitude, but I take this opportunity to acknowledge and appreciate their support.
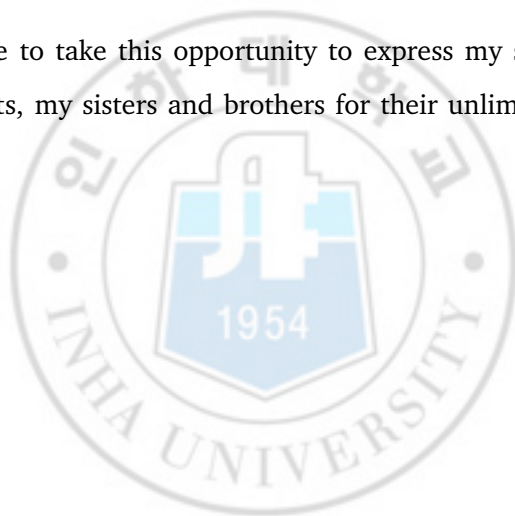
First of all, I would like to pay my sincere and deep gratitude to my academic supervisor Prof. Sang Sub Kim for his constant supporting and encouraging behavior, throughout this journey. He has always been available whenever I needed his help. This dissertation would not have seen the light of the day without his worthwhile support, insightful guidance and persistent help. I am thankful to him for his valuable suggestions and fruitful advices and for introducing me to several new and advanced areas of Nanomaterials and Nanotechnology. In fact, it was a great honor for me to work under his kind supervision.

I express my sincere and special thanks to Prof. Hyoun Woo Kim (Hanyang University, Korea) and Dr. Akash Katoch (India) for their valuable suggestions, fruitful discussions, encouragement and moral support at each and every step of this research. Without them, this research would not have been successful.

I would also like to thank my seniors (Jae Hyoung Lee and Jun Seong Lee) and colleagues (Jae Hun Kim, Zheng Yifang and Yu Jong Park) at the Nano Thin Film Laboratory for the friendly environment they provided me and for their support and care during my earlier days in Korea. They helped me a lot in adapting Korean culture and getting settled in Korea. I would like to thank Inha University for offering me a tuition fee scholarship that made my achievements possible.

I also want to thank all of my Pakistani and international friends at Inha University for providing me good company and helping me to settle in Korea smoothly and swiftly and for distracting me from work and making this journey enjoyable, especially Dr. Muhammad Aslam, Atta Ul Haq (Marie Curie Fellow, UK), Dr. Berindra Kumar (India), Dr. Ashadun Nobi (Bangladesh), Dr. Zeeshan Kaleem, Dr. Faiz Ali, Dr. Sabooh Ajaz (Australia), Dr. Fahd Nawaz Khan (UK), Farman Ali, Rizwan Ahmad, Tanveer Ranjha, Hamza Khan, and many more. Here, I would like to offer my special thanks to Dr. Pervez Khan for his extensive assistance and cooperation to make my stay comfortable.

I would also like to take this opportunity to express my sincerest love and thanks to my parents, my sisters and brothers for their unlimited support, love and best wishes.

Zain Ul Abideen
June 24, 2016

CONTENTS

LIST OF FIGURES

x

LIST OF TABLES

Chapter 1

Introduction

1.1 Overview

In recent years, research activities towards the development of chemically sensitive solid-state gas sensors at a nanometer scale have been enormously increased for better environmental control and safety. These gas sensor devices are utilized for practical applications ranging from toxic gas detection to manufacturing process monitoring, medical diagnostics to food processing and air quality monitoring to safety processes.

Resistive-type metal oxide based solid state gas sensors are the most widely studied, analyzed and used for practical applications among various other solid state chemical sensors (such as acoustics, optics, catalytic, work function based, electrochemical *etc*) [1]. The major advantages of metal oxide based gas sensors are their simplicity in use, small size, ease of fabrication, high sensitivity (can detect concentrations less than ppm levels) and low cost.

Shortly, after the discovery of the fact that the electrical properties of semiconductors change due to the interaction of gases on its surface [2–4], in the second half of the 20th century, Seiyama *et al.* [5] and Taguchi [6] were

the first to develop the metal oxide based resistive gas sensors. The most widely studied metal oxides for gas sensing applications are ZnO and SnO_2 because of their high sensitivity and stability. Many modifications have been proved to be effective to enhance the sensitivity, selectivity, stability and response speed of the metal oxides such as decreasing their size down to the nanoscale [7, 8], use of appropriate additives or dopants [9–11] and using synergistic effects of different metal oxides [12, 13]. Common dopants are transition metals (dispersed as ions in the oxide structure) or noble metals (Ag, Au, Pt, Pd *etc.*) which modify the electric properties of the metal oxides either by electronic sensitization [14] or by spillover effect [15, 16].

The methods to obtain selectivity in metal oxides can be classified into four groups: (i) the use of filters which discriminate between the gases on the basis of their chemical or physical properties (ii) the use of catalysts, promoters or surface additives (iii) use of temperature modulation and (iv) the physical preparation of the sensor material. The use of catalysts, promoters or additives and the use of temperature control are the most common techniques to obtain selectivity in metal oxides based gas sensors. However, the sensitivity and selectivity of the gas sensors by these methods were not enough to cope with the challenges in many specialized applications such as medical applications.

More recent studies have demonstrated that the use of composites or mixed metal oxides is another efficient and promising approach to improve the sensitivity, selectivity and other sensing parameters of metal oxide based gas sensors [17, 18]. These composite materials are likewise mentioned to as heterostructures and the physical interface between the dissimilar materials is referred to as heterojunction or heterointerface. The reason behind the improved sensing performance of the composite materials based sensors is the physical contact/heterointerface between the dissimilar materials, which makes the material system more conductive or resistive depending on their work functions or Fermi levels. As the implementation

of the nano materials [19] have improved the sensing performances as general, however, the use of nanoheterostructures have significantly amplified the overall performance of the gas sensors based on composite nanomaterials.

From various nanostructures, *one-dimensional* nanostructures (such as nanowires, nanobelts, nanotubes, nanofibers, and so on.), have several unique advantages such as large surface-to-volume ratio, small dimensions comparable to Debye length, superior stability when in the form of single crystal structure, ease of fabrication and funcionalization with target-specific receptor species, promoters or inhibitors of specific reactions can be easily deposited on the surface, and self heated devices can be prepared [20, 21]. Furthermore, they can be integrated with field-effect transistors (FET) configuration that allows the use of gate potential controlling the sensitivity and selectivity [22, 23].

However, among one-dimensional nanostructures, *nanofibers* have been identified as the most promising structure for high sensitivity and lower detection limits (sub-ppm level). They have relatively high surface-to-volume ratio than other one-dimensional nanostructures due to the presence of a large number of nanograins and a web like configuration and hence, are readily exposed to a large number of gas molecules, resulting in higher sensitivity and faster responses. Furthermore, nanofibers are generally synthesized by electrospinning which is a simple, low cost method and the control over processing parameters and on the characteristics of nanofibers is easy.

1.2 Synthesis of Metal Oxide Nanofibers

Metal oxide nanofibers are generally formed using same conventional methods which have been employed to produce polymeric fibers, which mainly involves the extrusion of a material by spinning to produce continuous nanofibers. Metal oxides are combined with a polymer, capable of fiber forming, and are converted

to a liquid state by heating, dissolution or pressurization. Although there are other techniques for fiber production such as phase separation, template synthesis, film splitting, drawing, thermal size-reduction, centrifugal spinning *etc*, capable of forming fibers from melts and solution, however, electrospinning is a highly flexible technique to produce long continuous nanofibers using solutions [24, 25], gels and liquid crystals [26], melts [27] and emulsions [28–30]. In literature, most of the composite metal oxide nanofibers for gas sensing applications reported have been synthesized by electrospinning combined with sol-gel method.

Electrospinning has many unique advantages over the other methods for the production of nanofibers or one-dimensional nanostructures. Nanofibers produced by electrospinning have extremely long length with a very high specific surface area and complex pore and web-like structure which are the necessary requirements for gas sensing applications. Composite metal oxides based gas sensors can be easily and massively produced on a commercial scale by straightforward, very low cost, versatile and facile electrospinning process. Here, it seems necessary to briefly explain the fundamentals and basic setup of the electrospinning process to synthesize the composite metal oxide nanofibers for gas sensing applications.

1.2.1 Electrospinning Process

Electrospinning is the most simple and versatile technique to generate various structures with different configurations such as normal, aligned, hollow, porous and core-shell of one-dimensional nanostructures from various materials even from ceramics [31, 32]. Electrospinning is a well-known process which was invented 80 years ago and has been extensively studied, analyzed and summarized [33]. Electrospinning involves the uni-axial stretching of a viscoelastic polymeric or melt solution based on electrostatic interactions (unlike a mechanical extension).

Electrospinning setup shown in Figure 1.1 basically consists of three components: a high voltage power supply (mostly DC but AC is also feasible [34]), a spinneret and a collector which is electrically conductive. The spinneret (a metallic needle) is attached with a plastic syringe which is loaded with the precursor/polymer solution. Since the quality and the final properties of nanofibers greatly depends on the quality and the size of the nanofibers, therefore the syringe is mostly connected with a syringe pump which enables to maintain a constant feeding rate of the solution through the spinneret. The collector is
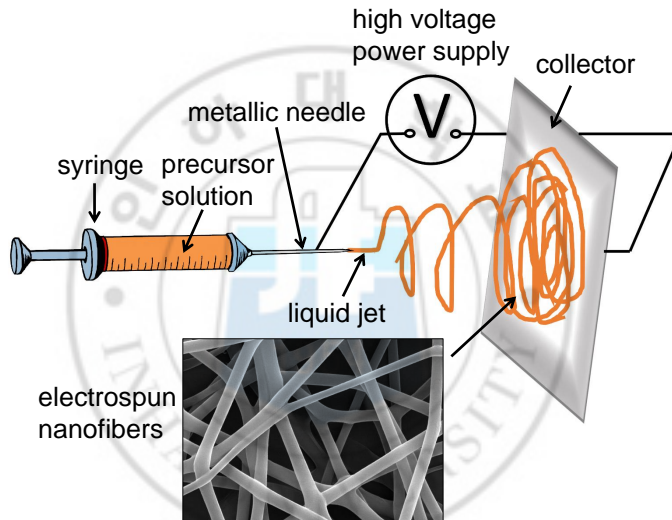
FIGURE 1.1: Schematic of an electrospinning process

usually an aluminum foil to collect the nanofibers but it can be of any material and in any configuration according to the required end product and it is positioned at a certain distance from the spinneret. This whole setup is usually enclosed in a box so that the environment or atmosphere (humidity *etc,*) can be controlled and varied according to requirements.

Under the applied high voltage (usually 1-30 KV), the drop at the needle tip deforms into a conical shape known as Taylor cone due to the presence of two major electrostatic forces: the electrostatic repulsion between the surface charges;

and the Coulombic forces exerted by the external electric field. After a certain threshold value, the applied electric field overcomes the surface tension of the solution and thus eject the drop from the needle towards the collector in the form of long and thin thread. During elongation and whipping, evaporation of some solvent also takes place which further reduces the diameter of the nanofibers. Using this extremely simple electrospinning process, nanofibers in the size range of a few micrometers to down to tens of nanometers can be produced.

Aside from the complex hydrodynamics involved in the electrospinning process [35–37], there are some process parameters, which greatly determine the morphology of the nanofibers. Major process parameters include viscosity and surface tension of the solution, applied voltage, feed rate, distance between spinneret and the collector, needle or nozzle size and the environment (humidity *etc*).

Metal oxides are mostly ceramics and cannot be directly spinnable although it is possible from their melt at extremely high temperatures. Thus, metal oxides have to rely on the use of precursor solutions. Figure 1.2 presents a complete procedure for the fabrication of composite ceramic nanofibers by electrospinning, with RGO-loaded ZnO composite nanofibers as an example. It consists of three major steps: (a) Preparation of an organic precursor solution containing alkoxide or salt with a polymer matrix. The compatibility and solubility of a
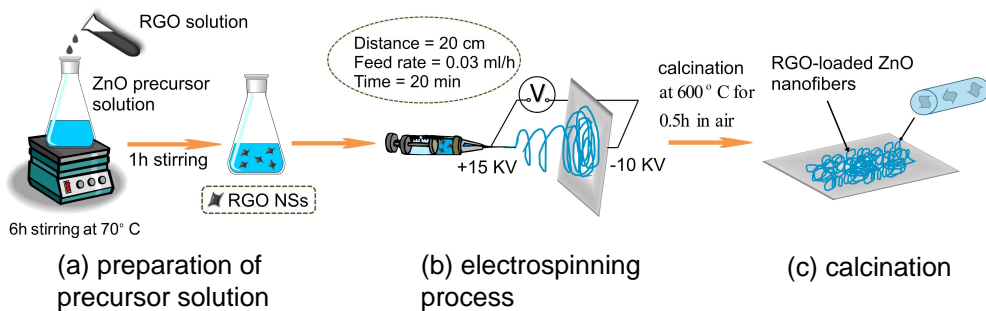
FIGURE 1.2: Fabrication process of composite metal oxide nanofibers

certain metal oxide with polymer solvent or precursor should be examined for required viscosity, before preparation of the solution. The most common polymers used to prepare metal oxides composite nanofibers with appropriate rheological properties are polyvinylpyrrolidone (PVP), polyvinyl acetate (PVAc), polyvinyl alcohol (PVA), polyacrylonitrile (PAN), and polyethylene oxide (PEO) [38]. (b) Electrospinning of the prepared solution to produce the composite nanofibers which also contain the polymer matrix or solvents. For metal oxide nanofibers, electrospinning process is usually carried out at room temperature in a controlled environment. (c) Calcination or sintering of electrospun nanofibers at elevated temperatures to obtain the desired precursor nanofibers by evaporating the all organic components. The diameter of calcined nanofibers is generally smaller than as-spun nanofibers due to the loss of the polymeric solvents during calcination process.

Moreover, extremely small grains, called nanograins, evolve on the nanofibers during calcination process which play a significant role in the resultant gas sensing properties of the nanofibers. The size of the nanograins can be manipulated and changed according to the desired applications of the nanofibers by controlling the heat treatment conditions (heating temperature, heating time, heating rate, cooling rate *etc*). For gas sensing applications, the size of the nanograins must be optimized to get best sensing performances and results. Usually, nanofibers with smaller nanograins show better sensitivity and quicker response than those with the larger nanograins. Furthermore, nanograins on nanofibers also influence their electrical transport, magnetic, optical and photocatalytic properties, in addition, to their gas sensing properties [39]. A number of composite oxides based nanofibers that include CuO-SnO_2 [40], ZnO-CuO [41], TiO_2-ZnO [42, 43], p-NiO/n-SnO_2 [44], ZnO-In_2O_3 bi-layer [45, 46], In_2O_3-WO_3 [47], La_2O_3-WO_3 [48], SnO_2-CeO_2 [49], SnO_2/In_2O_3 [50], ZnO/In_2O_3/ZnO tri-layer [45], $In_{2-x}Ni_xO_3$ [51] *etc,* have been prepared by electrospinning process

for gas sensing applications.

1.2.2 Fabrication of Sensor Devices

After calcination of nanofibers, which were deposited on ceramic substrates (SiO_2 or Si), electrodes are made by the deposition of a highly conductive metal (mostly Au or Pt) usually by sputtering on the nanofibers in a well-controlled environment using interdigitated electrode masks (IDE masks). An intermediate layer (usually
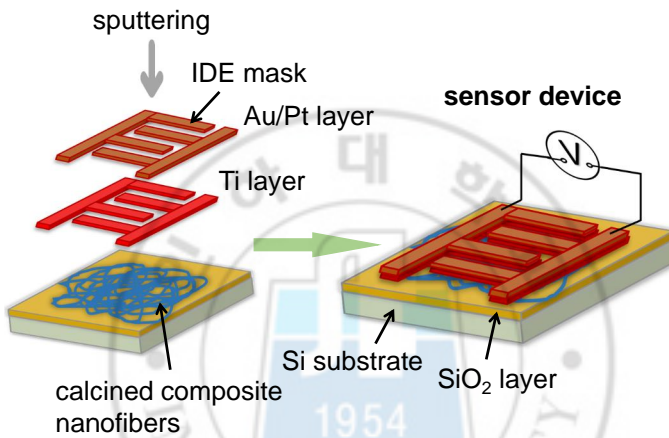
FIGURE 1.3: A typical configuration of a sensor device

Ti) is also deposited which acts as an adhesive layer between Si/SiO_2 and Pt layer. A typical sensor device fabricated by composite nanofibers is shown in Figure 1.3. These metal layers act as electrodes for the measurement of electrical properties. Another part of a gas sensor is the heating layer which is separated from sensing and electrode layers by an insulating layer.

1.3 Applications of Chemical Gas Sensors

Chemical gas sensors have found their applications in the variety of fields. Some of them are listed below,

1. Harmful chemicals detection

2. Environmental monitoring

3. Chemical weapons detection

4. Space applications

5. Security and emergency applications

6. Food processing and quality

7. Home and industrial safety

8. For specialized applications such as high temperature gas sensing

9. Detection of harmful gases in mines

10. Non-invasive medical diagnostics such as breath analysis

However, here, the author would like to briefly highlight the most important application of the chemical gas sensors in the following section.

1.3.1 Detection of Disease through Exhaled Breath Analysis

Among various possible applications of highly sensitive electrospun composite nanofibers based gas sensors, detection of a disease through human breath is the most potential application of these highly sensitive gas sensors. Exhaled breath is a complex mixture of volatile and non-volatile organic compounds. The primary components of exhaled breath, other than air, are water vapor, hydrogen, ammonia, carbon monoxide, methane (in the range of parts per million (ppm)) and trace amounts of volatile organic compounds (VOCs) such as acetone, methanol, pentane, isoprene, ethanol and many other metabolite compounds, typically in the range of parts per billion (ppb) or parts per trillion (ppt) range [52, 53]. In addition to exhaled breath, VOCs are also present in other body fluids such as blood, urine, stool and sweat [54–56]. Different VOCs have

9

been correlated with different specific diseases because it is assumed that the consequences of disease include the generation of new VOCs and/or alteration of the concentrations of existing VOCs. Hence, the selective detection of VOCs may serve as biomarkers for assessment or detection of disease [57]. Breath analysis for disease detection through VOCs has a long history (since 1971) [56] and it has been demonstrated that various serious and fatal diseases such as different types of cancer, multiple sclerosis, Parkinson's and Alzheimer's disease, tuberculosis, diabetes, and chronic kidney diseases can be detected via VOCs present in breath [58, 59]. Several reviews can be consulted for the detailed study of VOCs detection, breath sampling and biomarkers related to specific disease [60–62]. However, an overview of the processes involved in the exhaled breath analysis is presented in Figure 1.4 [59].
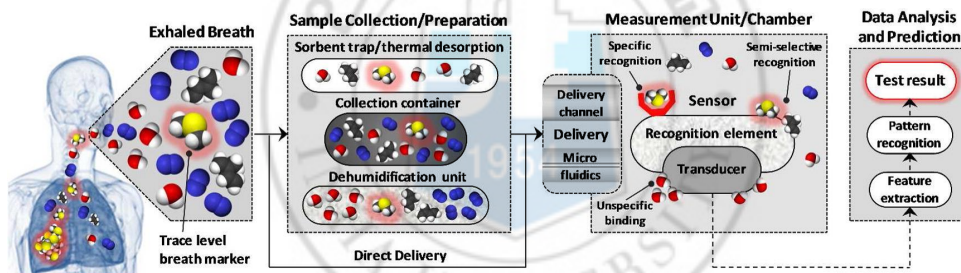
FIGURE 1.4: Processes involved in the exhaled breath analysis

Among several other VOCs detection techniques such as various gas chromatography or mass spectroscopy techniques, laser spectroscopy, proton-transfer reaction-mass spectroscopy (PTR-MS), selected ion flow tube-mass spectroscopy (SIFT-MS), chemical gas sensors based on nanomaterials have shown promising results for the detection of biomarkers in exhaled breath [58, 63]. This can be attributed to the high sensitivity, low cost, controllable properties, low power consumption, portability and simplicity of nanostructured chemical gas sensors. In this regard, electron noses (arrays of sensors) offer cheap and highly selective detection of gases in the presence of gaseous mixtures

or background gases, enabling detection of multianalyte gases through pattern recognition. Metal oxide electrospun nanofibers based gas sensors for VOCs detection are still in development and are showing their potential for this application.

Nevertheless, the detection of trace amounts of a mixture of VOCs present in the exhaled breath which also carry high degrees of humidity (40-80%) with nanofibers based gas detectors is really challenging. An ideal gas sensor for breath analysis should have extremely high sensitivity (in the ppb level range), selectivity, tolerance for variable chemical and humidity backgrounds, room temperature operation, low cost and should respond rapidly and differently to small changes of VOCs concentrations. Furthermore, it should have consistency in the output and should come back to its baseline when not in contact with the VOCs. In this regard, gas sensors comprised of metal oxide electrospun nanofibers can be an important and promising tool for next-generation non-invasive medical diagnostic applications, mainly because of their high surface to volume ratio, large depletion region, the synergistic behavior of different components, detection ability of a diverse range of analyses. However, still many technological advancements in terms of material selection and their fabrication, need to be made.

Careful selection of different materials, morphologies, functionalization of composites with dopants or catalysts, temperature modulation and further clarification of their sensing mechanism may enhance the sensing performance of electrospun composite nanofibers based sensors and allow the selective and rapid detection of specific biomarkers related to specific diseases. Electron noses (arrays of sensors) based on electrospun composite nanofibers would additionally improve the precision, flexibility, portability and cost efficiency.

1.4   Thesis Organization

The remainder of this thesis is primarily devoted to the investigation of the gas sensing characteristics and sensing mechanism of graphene loaded SnO_2 and reduced graphene oxide loaded ZnO nanofibers. A brief background, detailed fabrication procedures and sensing mechanisms are discussed in every chapter. Thesis organization is as follows:

Chapter 2 addresses in detail about the characterization and analysis of gas sensing performance of graphene loaded SnO_2 composite nanofibers. The evaluation of graphene content and the operating temperature is also discussed in this chapter. Sensing mechanism related to this novel sensor is discussed in detail according to the sensing results. The comparison of sensing properties of graphene loaded SnO_2 nanofibers with pristine SnO_2 nanofibers is also presented.

Chapter 3 describes and develops fundamentals regarding reduced graphene oxide loaded ZnO nanofibers. In this chapter, the overall general fabrication, characterization analysis and sensing mechanisms related to reduced graphene oxide loaded ZnO nanofibers is presented in detail. However, the main theme of this chapter is to develop an extremely sensitive gas sensor and to optimize the content of reduced graphene oxide nanosheets in the ZnO nanofibers. The sensing properties of reduced graphene oxide loaded ZnO nanofibers are also compared with pristine ZnO nanofibers.

Chapter 4 is devoted completely for the Hydrogen gas detection of reduced graphene oxide loaded ZnO nanofibers. Hydrogen sensing characteristics at various temperatures, effect of temperature and stability of the sensors is discussed in this chapter. In the end, various possible reasons are discussed in detail as sensing mechanism for the exceptionally high sensitivity and selectivity of reduced graphene oxide loaded ZnO nanofibers for hydrogen gas. Hydrogen sensing properties of reduded graphene oxide loaded ZnO, reduced graphene oxide loaded

SnO_2, pristine ZnO and pristine SnO_2 are also compared.

Chapter 5, finally, presents detailed conclusions drawn from this research. Various possibilities for the future work are also suggested.

Chapter 2

Graphene-loaded SnO$_2$ Composite Nanofibers

In the first chapter, we presented an overview of the chemical gas sensors based on composite nanomaterials and their significance. In this chapter, the gas sensing properties of graphene-loaded SnO$_2$ composite nanofibers synthesized by a low cost facile electrospinning process with concentrations of graphene (ranging from 0.05 to 1.5 wt%) will be discussed. Trace concentrations (1, 3, and 5 ppm) of various reducing gases (C$_6$H$_6$, C$_7$H$_8$, CO, CO$_2$, and H$_2$S) were tested at temperatures between 200 and 400 °C. The graphene-loaded SnO$_2$ composite nanofibers showed excellent and enhanced sensitivity, as compared to pristine SnO$_2$ nanofibers, with the optimal amount of graphene being 0.5 wt%. The graphene-loaded SnO$_2$ composite nanofibers exhibited a high sensor response of 11.6 with a short response time of 3.2 s (at 5 ppm of H$_2$S gas). A novel sensing mechanism for the excellent sensitivity of the graphene-loaded SnO$_2$ composite nanofibers will also be presented in detail.

2.1 Introduction

Tin dioxide (SnO$_2$) is a well-known *n*-type semiconductor with a large band gap of 3.6 eV. It has been widely studied for gas sensing applications because of its good chemical and thermal stability, high carrier density, and good response to various types of toxic gases and organic vapors. Moreover, its stability at higher temperatures makes using SnO$_2$ possible in harsh environments where explosive gases might exist. Therefore, much of the research in the field of gas-sensors still focuses on methods to further enhance the sensitivity and selectivity of SnO$_2$-based gas sensors. This is typically done by controlling the nanostructure morphology and incorporating various additive materials. Since the morphology and surface state play a significant role in changing the characteristics of sensing materials, different nanostructural configurations and surface morphologies have been widely studied in attempts to meet the high sensitivity requirements [64].

In this regard, *one-dimensional* SnO$_2$ nanostructures, such as nanowires, nanotubes, nanofibers, nanobelts, nanorods, *etc*, have shown outstanding chemical sensing performances relative to their bulk counterparts. This difference in performance is caused by the specific physical and chemical properties, which are generally influenced by the high specific surface area and confined directional carrier support. However, nanofibers synthesized by electrospinning possess additional unique features such as web-like morphologies, which enable gas molecules to readily interact with and diffuse effectively into all of the nanofibers simultaneously. This enhances the reaction speed and sensitivity. Additionally, the presence of nanograins in the nanofibers provides additional reaction sites and resistance modulation due to the enormous number of grain boundaries. Furthermore, electrospun nanofibers have high reproducibility and good stability at higher temperatures.

Therefore, SnO$_2$ nanofibers are potential candidates for future electronic and

gas sensing devices [30]. One of the other commonly and widely employed techniques used to enhance the sensitivity or selectivity is the incorporation of effective additive materials into the sensing host material. In this regard, many types of additives, including noble metals, transition metals, semiconducting or semimetal elements, light elements, rare-earth elements, and organic materials, have been included in SnO$_2$ hosts and extensively studied for the sensing of various oxidizing and reducing gases [65].

Among these, graphitic nanocarbons (particularly graphene) have recently attracted extraordinary attention in the gas sensor community because of their unique properties [66–68]. For instance, graphene is a two-dimensional monolayer sheet of sp^2-bonded carbon atoms that is densely packed in a honeycomb-like structure. This structure provides a large theoretical specific surface area (2630 m^2 g^{-1}) [69, 70]. All atoms of graphene can be considered to be surface atoms that are readily exposed to the target gas. Furthermore, graphene has high thermal stability, excellent electrical conductivity, good mechanical strength, high carrier mobility, and extremely low electrical noise. As a result, a small amount of electrons can produce a noticeable change in the conductance of graphene [71]. All of these characteristics make graphene an attractive material for gas sensing applications. In fact, graphene-based sensors have been widely used to detect poisonous and explosive gases [72–74]. Moreover, graphene-loaded SnO$_2$ composites have been shown to be efficient gas sensors due to their improved gas response, selectivity, response/recovery times, and low operating temperatures.

However, to understand the enhancement mechanism (in regard to the addition of graphene nanosheets) and to obtain the maximum sensitivity, the amount and/or dispersion of graphene nanosheets must be optimized. This optimization is also important from the viewpoint of gas selectivity. In this study, we investigate and report on the enhanced sensing performances of SnO$_2$

nanofibers that are caused by the addition of graphene nanofibers. To date, no study has investigated the sensing properties of graphene-loaded SnO$_2$ composite *nanofibers*. We investigated the effects of graphene loading into SnO$_2$ nanofibers, optimized the amount of graphene nanosheets for high sensitivity, characterized the gas sensing properties (with very low gas concentrations) at various temperatures (200-400 °C), and compared the sensing results of graphene-loaded SnO$_2$ composite nanofibers with those of pristine SnO$_2$ nanofibers. Finally, the sensing mechanism that is responsible for the enhanced sensing performance of the graphene-loaded SnO$_2$ composite nanofibers is proposed and discussed. The sensing performance was characterized as a function of the graphene content and operating temperature with various gases. Our results show that the graphene-loaded SnO$_2$ composite is a promising material system that can be used to develop extremely sensitive gas sensors.

2.2   Experimental Details

2.2.1   Materials

Tin(II) chloride dehydrate (SnCl$_2$.2H$_2$O), polyvinyl acetate (PVAc, Mw = 850,000), ethanol (anhydrous, 99.5%), dimethylformamide (DMF, 99.8%), graphene, and de-ionized water were used as the starting materials. All materials were purchased from Sigma-Aldrich Corp.   and were used without further purification or refining.

2.2.2   Synthesis and Characterization of Graphene

As a source material, 1 g of expandable graphite (Hyundai Coma Industry) was put into an alumina crucible. The reaction products were irradiated by rapid microwave heating for 1 min with a frequency and power of 60 Hz and 1000

W, respectively. The exfoliated graphite was sonicated in ethanol for 10 min and subsequently dried in a vacuum oven. The sonication and drying processes were repeated three times to obtain graphene flakes that consisted of a few layers. More details about the synthesis and characterization procedures that were used in the present study can be found in our previous reports [75, 76].

2.2.3   Synthesis of Graphene-loaded SnO$_2$ Composite Nanofibers

The graphene-loaded SnO$_2$ composite nanofibers were synthesized using electrospinning. First, PVAc was dissolved in a mixed solvent consisting of equal amounts of ethanol and DMF; this was continuously stirred for 4 h. Subsequently, SnCl$_2$.2H$_2$O and the graphene solution were added to the PVAc solution and stirred continuously for 12 h without heating. The prepared viscous solution was loaded into a syringe equipped with a 21-gauge stainless steel needle with an inner diameter of 0.51 mm. The feed rate, applied voltage, and distance between the tip of the syringe needle and the aluminum collector were fixed at 0.03 mL/h, 15 kV, and 20 cm, respectively.

All of the electrospinning experiments were performed at room temperature in air. The nanofibers were collected uniformly over SiO$_2$-grown (thickness $\sim$ 250 nm) Si wafers that were placed on the collector. The prepared electrospun nanofibers were calcined at 600 °C in air for 30 min at a heating rate of 5 °C/min. The same procedure was adopted to synthesize the graphene-loaded SnO$_2$ composite nanofibers with different contents of graphene (0.05, 0.1, 0.3, 0.5, 1, and 1.5 wt%). Further details of the procedure used to synthesize electrospun SnO$_2$ nanofibers are provided in our earlier reports [77, 78].

2.2.4 Microstructural and Sensing Characterization

The microstructure and phase composition of the synthesized graphene-loaded SnO$_2$ composite nanofibers were investigated by field-emission scanning electron microcopy (FE-SEM, Hitachi S-4200) and high-resolution transmission electron microscopy (HR-TEM, Phillips CM-200). For FE-SEM, the samples were cleaned by several steps (ultrasonic cleaning, blow-drying, and drying using an oven or hot plate). They were then sputter-coated with a Pt layer in order to eliminate the charge effect. For HR-TEM, the samples were ultrasonically dispersed in acetone. Subsequently, drops of the suspension were deposited on amorphous carbon films supported on copper grids and dried in air.

To investigate the sensing behavior of graphene-loaded SnO$_2$ composite nanofibers, double layer electrodes of Ti (thickness $\sim$ 50 nm) and Pt (thickness $\sim$ 200 nm) were sequentially deposited onto the specimens using radio frequency magnetron sputtering at room temperature. The complete procedures used for the synthesis of graphene-loaded SnO$_2$ composite nanofibers using electrospinning and the fabrication of sensing devices are shown in Figure 2.1.

Afterwards, the gas sensing properties of the graphene-loaded SnO$_2$ composite nanofiber sensors towards various reducing gases (CO, C$_7$H$_8$, C$_6$H$_6$, CO$_2$, and
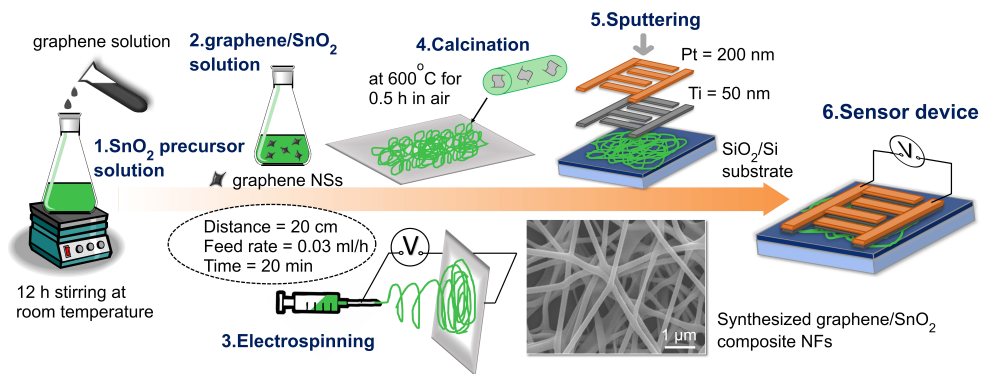
FIGURE 2.1: Schematic illustration of the synthesis of graphene-loaded SnO$_2$ composite nanofibers

H$_2$S) at concentrations ranging from 1-5 ppm were measured under atmospheric conditions at an operating temperature between 200 and 400 °C. Measurements were conducted using a homemade gas dilution and sensing system. The sensors were placed and evaluated in a testing chamber at constant temperatures and the operating temperature of the sensors was controlled by using an external heating source. Details of sensor design, gas dilution, and the sensing system are provided in our earlier reports [42, 79]. The sensors were stabilized for ~20 min in the baseline gas (synthetic dry air) to obtain a stable resistance at every operating temperature (prior to the gas sensing tests). The gas concentration was precisely controlled by changing the mixing ratio of the dry air-balanced target gas and the synthetic dry air through accurate mass flow controllers. The response of the sensors to the reducing gas is defined as the ratio of R$_a$ to R$_g$. Here, R$_a$ is the original base resistance of the sensor in air and R$_g$ is the stabilized resistance of the sensor in the presence of the applied gas. The response time (τ_{res}) is defined as the time in which the resistance of the sensor changes to 90% of the original base resistance and the recovery time (τ_{rec}) is defined as the time needed until 90% of the signal is recovered.

2.3   Results and Discussion

2.3.1   Microstructural Analysis

Figure 2.2 shows the typical microstructures of the calcined graphene-loaded SnO$_2$ composite nanofibers containing various amounts of graphene nanosheets. The average diameter of the calcined nanofibers is measured to be about 200-300 nm and the lengths are in the range of several micrometers. However, it is seen that the size of the nanograins and/or the diameter of the nanofibers are not significantly affected by varying the graphene content. The presence of nanograins on the nanofibers can be clearly seen; these are evolved during the calcination
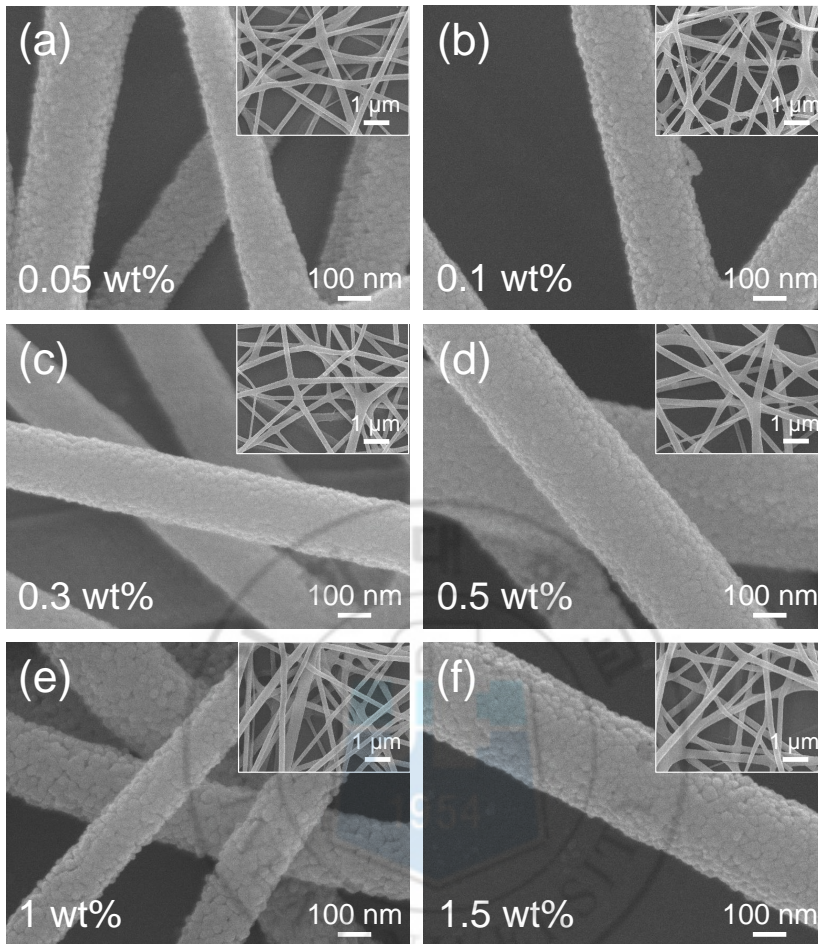
FIGURE 2.2: SEM of the graphene-loaded SnO$_2$ composite nanofibers with various graphene contents

process. The upper-right insets show that the nanofibers are uniformly and randomly distributed on the SiO$_2$/Si substrates.

The polycrystalline nature of SnO$_2$ nanofibers (Figure 2.3a) along with the presence of graphene nanosheets (Figure 2.3b-c) is confirmed by HR-TEM. Figure 2.3b-c show the presence of graphene sheets along with the nanograins of the nanofibers. It can be seen that nanofibers are anchored and largely dispersed on larger graphene nanosheets (Figure 2.3b), while some of the graphene sheets are folded in between the nanograins of the nanofibers (Figure 2.3c); this
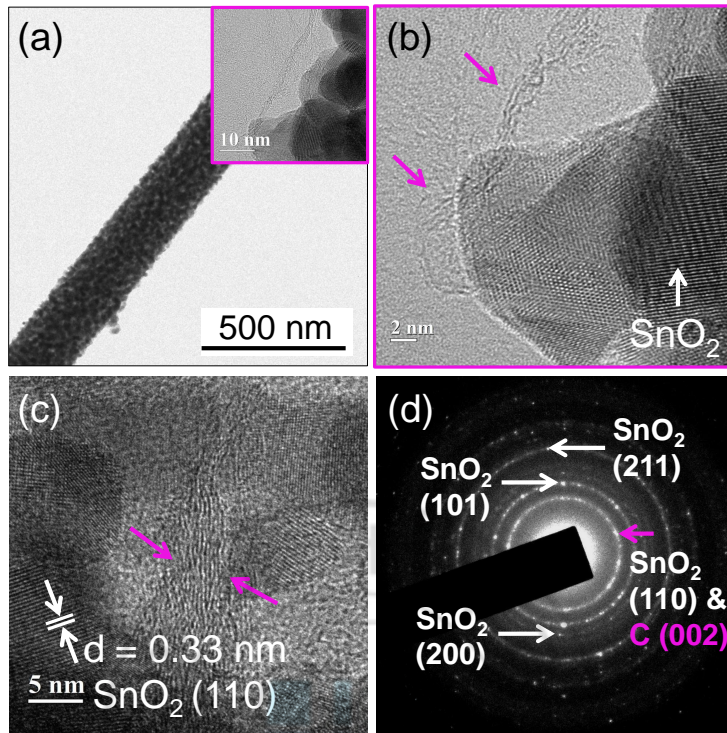
FIGURE 2.3: Microstructural analysis of graphene-loaded SnO$_2$ composite nanofibers

confirms the multilayer graphene configuration. Understanding these kinds of interactions between graphene nanosheets and SnO$_2$ nanofibers is important in order to understand the electrical transport properties and sensing mechanism of graphene-loaded SnO$_2$ composite nanofibers; this will be discussed in the following paragraphs. The inter-planar distance of the SnO$_2$ nanofibers is 0.33 nm, which corresponds to the (110) crystallographic plane of the rutile SnO$_2$ phase. Figure 2.3d shows the selected area diffraction ring patterns of graphene-loaded SnO$_2$ composite nanofibers. These can be indexed to the rutile SnO$_2$ structure (JCPDS Card No. 41-1445). The weakness and invisibility of graphene-related patterns is associated with the low graphene content. However, it is possible that there exists a ring pattern that could be indexed to the (002) plane of 2H graphite (JCPDS Card No. 75-1621), which overlaps with the (110)

plane of the rutile SnO$_2$ structure. From Figure 2.3, we can conclude that we successfully synthesized graphene-loaded SnO$_2$ composite nanofibers.

2.3.2   Gas Sensing Results

In order to examine and compare the sensing properties of graphene-loaded SnO$_2$ composite nanofibers with pristine SnO$_2$ nanofibers, we first expose the sensors to trace concentrations (1, 3, and 5 ppm) of a relatively weak reducing gas (C$_7$H$_8$) at a preliminary temperature of 300 °C. This is done to investigate the effect of loading graphene and to select the optimal amount of graphene nanosheets in the SnO$_2$ nanofibers needed to obtain the maximum response (as compared to the rest of the sensors). The dynamic resistance curves of the pristine SnO$_2$ and graphene-loaded SnO$_2$ composite nanofibers, containing various amounts of graphene (0.05, 0.1, 0.3, 0.5, 1, and 1.5 wt%), are shown as a function of the gas concentration in Figure 2.4a. The resistance of the sensors decreased upon exposure to the C$_7$H$_8$ and returned back to its base resistance upon removal of the gas.

The sensing behavior of the graphene-loaded SnO$_2$ composite nanofibers was similar to that of a typical *n*-type material-based gas sensor (*i.e*, a decrease in the resistance upon introduction of a reducing gas). This suggests that the electrical conductivity mainly occurred through the *n*-type SnO$_2$ semiconducting oxide as opposed to through the *p*-type graphene nanosheets; this is likely caused by the low content of graphene. The responses of all of the sensors to C$_7$H$_8$ gas at 300 °C are shown in Figure 2.4b. The response of the sensors increases as the gas concentration increases. It is also clear that the graphene-loaded SnO$_2$ composite nanofibers was more sensitive to trace concentrations of the gas as compared to the pristine SnO$_2$ nanofibers at the same operating temperature. However, the optimal amount of graphene was observed to be 0.5 wt% with the highest response of 3.13 and a very short response time of 51.2 s, as compared to the rest
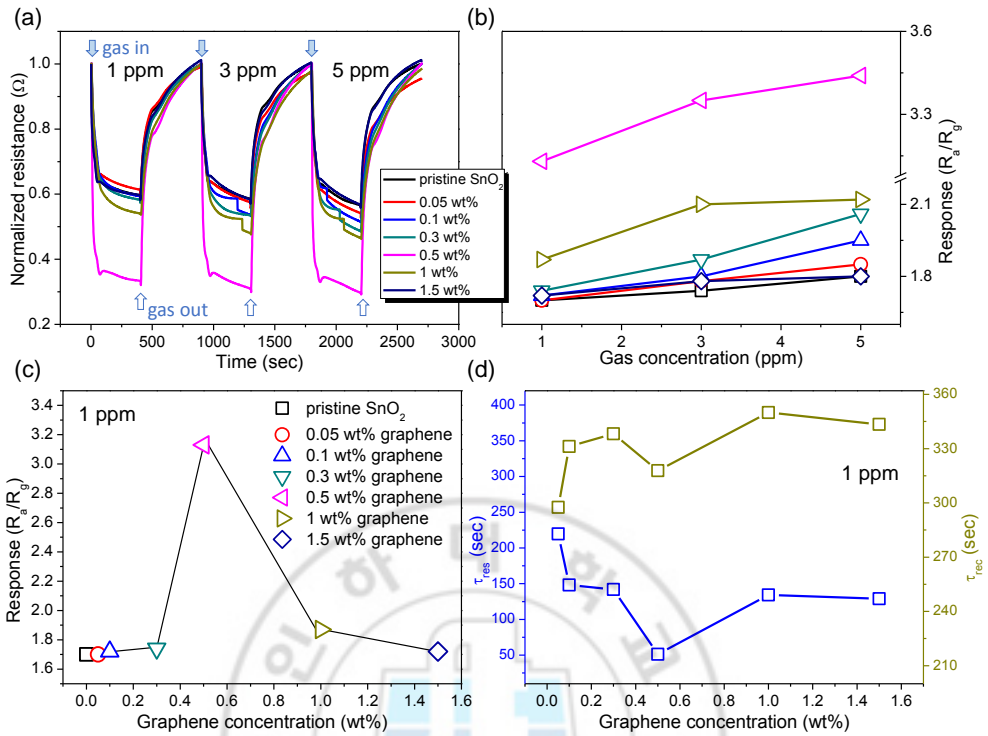
FIGURE 2.4: Summarized Resistance curves, responses and response and recovery times of the pristine SnO$_2$ and graphene-loaded SnO$_2$ composite nanofibers at 300 °C

of the sensors (at 1 ppm of C$_7$H$_8$ gas at 300 °C; Figure 2.4c-d). In contrast, the response of pristine SnO$_2$ nanofibers was 1.7 with a response time of 125 s. The response of graphene-loaded SnO$_2$ composite nanofibers increased by 84.1% and had an improved response time relative to SnO$_2$ nanofibers. The response and recovery times of all sensors to 1 ppm of C$_7$H$_8$ are shown in Figure 2.4d. The shortest response time was attained by inserting 0.5 wt% of graphene. However, with more than 0.5 wt% of graphene, the response of the sensors decreased significantly. Following this, all the remaining sensing experiments were carried out with sensors containing the optimized amount of graphene (0.5 wt%). The bell-shaped response behavior as a function of the graphene concentration is discussed after establishing the sensing mechanism of graphene-loaded SnO$_2$
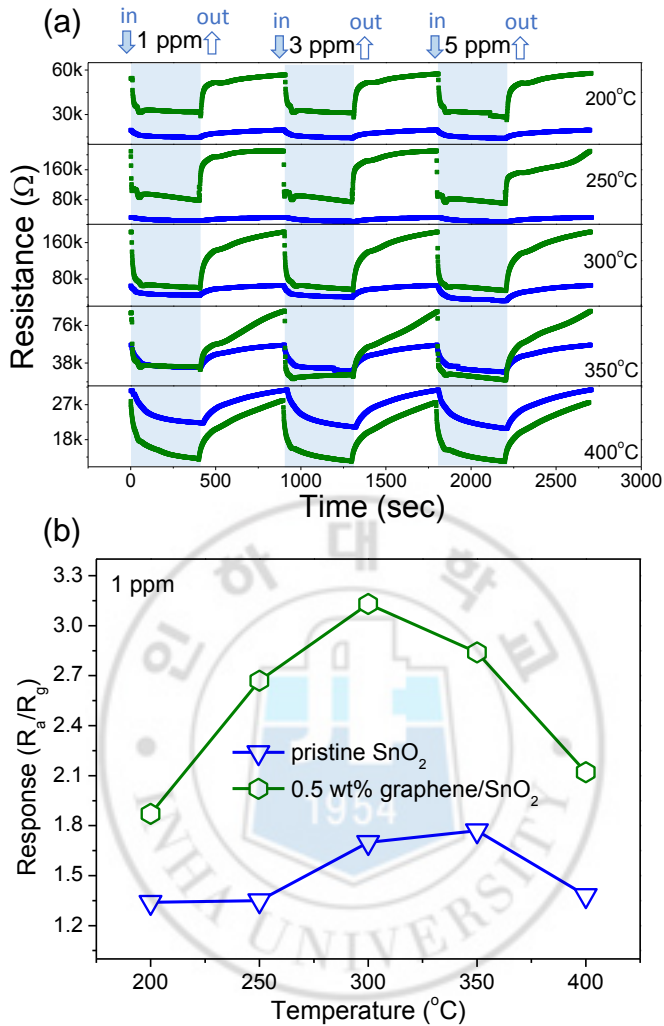
FIGURE 2.5: Resistance curves and responses of pristine SnO$_2$ and 0.5 wt% graphene-loaded SnO$_2$ composite nanofibers as a function of temperature

composite nanofibers.

To investigate the effect of the operating temperature, the graphene-loaded SnO$_2$ composite nanofibers and pristine SnO$_2$ nanofibers were exposed to C$_7$H$_8$ gas at various temperatures (200, 250, 300, 350, and 400 °C) (Figure 2.5a). Figure 2.5b shows the responses of pristine SnO$_2$ and graphene-loaded SnO$_2$ composite nanofibers to 1 ppm of C$_7$H$_8$ gas at different temperatures. The

responses of the graphene-loaded SnO$_2$ composite nanofibers were significantly higher than the pristine SnO$_2$ nanofibers for all temperatures.   It is also clear that graphene-loaded SnO$_2$ composite nanofibers showed an increased response at lower temperatures with a maximum response of 3.13 at 300 °C; the response becomes less sensitive at higher temperatures.   In contrast to graphene-loaded SnO$_2$ composite nanofibers, pristine SnO$_2$ nanofibers showed a maximum response of 1.77 at an operating temperature of 350 °C. The response of the graphene-loaded SnO$_2$ nanofibers was 76.8% higher than that of the pristine SnO$_2$ nanofibers at their respective optimal temperatures.   The responses of both pristine SnO$_2$ and graphene-loaded SnO$_2$ composite nanofibers exhibited bell-shaped behavior, which is consistent with the literature. This trend, which possesses a volcano shape, is observed to increase in height and shift towards lower temperatures when the semiconductor materials were loaded with catalyst materials (*e.g*, transition metal, graphene, *etc*). Similar trends were also reported elsewhere [78, 80–82] in a variety of sensor systems, including SnO$_2$ with respect to H$_2$ gas [83], CdIn$_2$O$_3$ nanocrystals with respect to ethanol gas [84], and Au-functionalized reduced graphene oxide-loaded SnO$_2$ nanofibers with respect to CO gas [82].   It is expected that chemical reactions will not be facilitated at temperatures that are too low, whereas adsorption will be suppressed at temperatures that are too high.

In order to investigate the selectivity and the effect of interfering gases, graphene-loaded SnO$_2$ composite nanofibers were tested for other reducing and toxic gases, such as C$_6$H$_6$, C$_7$H$_8$, CO, CO$_2$, and H$_2$S, at the optimal operating temperature.   The gas concentration was kept very low, ranging from 1 to 5 ppm, as summarized in Figure 2.6.   The dynamic resistance curves of 0.5 wt% graphene-loaded SnO$_2$ composite nanofibers are shown in Figure 2.6a.   Figure 2.6b shows the responses of graphene-loaded SnO$_2$ composite nanofibers to 1 ppm of gases relative to the responses of pristine SnO$_2$
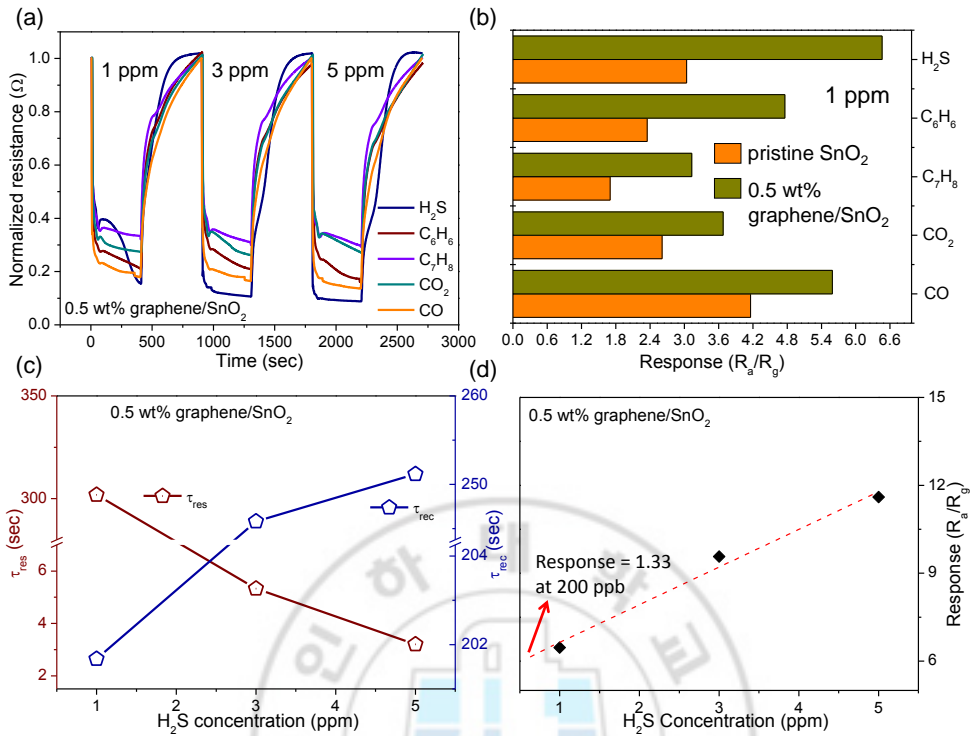
FIGURE 2.6: Resistance curves and responses of 0.5 wt% graphene/SnO_2 composite and pristine SnO_2 nanofibers for various gases

nanofibers. Graphene-loaded SnO_2 composite nanofibers showed significantly higher responses than those of pristine SnO_2 nanofibers. However, significant selectivity towards a particular gas was not observed; this is probably due to the very low concentration of gases. However, analysis of the results revealed that the graphene-loaded SnO_2 sensors were quite selective for H_2S gas at higher concentrations. The response of graphene-loaded SnO_2 compoiste nanofibers for 1 ppm of H_2S is 6.46, which is 112.5% higher than that of pristine SnO_2 nanofibers (Figure 2.6b). Moreover, an increase of 134.3% in the response, as compared to pristine SnO_2 nanofibers, was observed at 5 ppm of H_2S at the same optimal temperature (Table 2.1). Graphene-loaded SnO_2 sensors showed an H_2S response of 11.6 with an extremely short response time of 3.2 s.

28

TABLE 2.1: Responses of graphene loaded SnO$_2$ composite nanofibers

Gas concentration	Pristine SnO$_2$ nanofibers		0.5 wt% graphene/SnO$_2$ composite	
	(1 ppm)	(5 ppm)	(1 ppm)	(5 ppm)
CO	4.16	4.79	5.59	7.34
CO$_2$	2.61	2.92	3.68	3.77
C$_7$H$_8$	1.7	1.8	3.13	3.44
C$_6$H$_6$	2.35	2.5	4.76	6.2
H$_2$S	3.04	4.95	6.46	11.6

The response and recovery times of graphene-loaded SnO$_2$ composite nanofibers for H$_2$S are presented in Figure 2.6c. In the case of gas sensors used in medical applications, such as for the diagnosis of halitosis via breath analysis, at least 1 ppm of H$_2$S should be detected; this is the concentration where odor becomes recognizable in the exhaled breath of halitosis patients [85]. However, the lower limit of detection (LOD) for 0.5 wt% graphene-loaded SnO$_2$ composite nanofibers for H$_2$S was estimated using linear extrapolation. The results show that 0.5 wt% graphene-loaded SnO$_2$ composite nanofibers were able to detect as little as 200 ppb of H$_2$S with a response of 1.33 (at an operating temperature of 300 °C). This means the concentration of H$_2$S (1 ppm) that is present in the exhaled breath of halitosis patients is within the detectable range (Figure 2.6d).

2.3.3   Sensing Mechanism

In order to understand the sensing mechanism of graphene-loaded SnO$_2$ nanofibers, we first explain the sensing mechanism of nanofibers made of *n*-type materials (such as SnO$_2$). The higher sensitivity of nanofibers is typically attributed to the resistance modulation that arises from the following mechanisms. First, there is the modulation of the resistance along the surface of the nanofibers. Secondly, the resistance modulation arises because of potential barriers, which develop at the grain boundaries of the nanograins of nanofibers. In air ambient conditions, oxygen molecules adsorb, diffuse, and trap electrons at the

surface/grain boundaries of the nanofibers to form atomic and molecular ions (O$^-$, O^{2-}, *etc*). An electron depletion region is established underneath the surface/grain boundaries due to the extraction of electrons by these adsorbed ions.

When reducing analytes (*e.g*, H$_2$S) are inserted, the reducing gas molecules react with the chemisorbed oxygen at the surface and grain boundaries of the nanofibers and donate electrons that were trapped by the chemisorbed oxygen back to the conduction band; this reduces the potential barriers and increases the conductivity. In the case of H$_2$S, the pre-adsorbed oxygen releases in the form of H$_2$O and SO$_2$ according to the reaction $H_2S_{(g)} + 3\,O^- \longrightarrow SO_{2(g)} + H_2O_{(g)} + 3\,e^-$. These sensing mechanisms typically operate in *n*-type metal oxide-based gas sensors with nanofibrous structures. Our experimental results were also consistent with the aforementioned mechanism; the resistance of the pristine SnO$_2$ nanofibers decreased upon introduction of reducing gases (*e.g*, H$_2$S).

Additionally, high sensitivity with a very short response time towards H$_2$S suggests that the electron transfer at H$_2$S/SnO$_2$ interfaces is increased due to the excellent electron transfer capabilities of graphene. Graphene nanosheets may also help prevent the agglomeration of nanofibers, as compared to pristine SnO$_2$ nanofibers, which would enhance the overall adsorption and diffusion of H$_2$S gas molecules. In this way, the presence of graphene increases the overall electronic sensitization. The strong interaction between H$_2$S and defective graphene (H$_2$S interaction with graphene is observed to increase when Stone-Wales defects are present in graphene) has also been studied and observed by other research groups [86–88]. It is possible that graphene plays a catalytic role in enhancing the sensing behaviors by means of the spillover effect.

Furthermore, additional sources for the sensitivity enhancement of graphene-loaded SnO$_2$ composite nanofibers are related to the graphene/SnO$_2$ heterointerfaces (Figure 2.7). In the heterojunctions, the work functions of

(a)

(b)
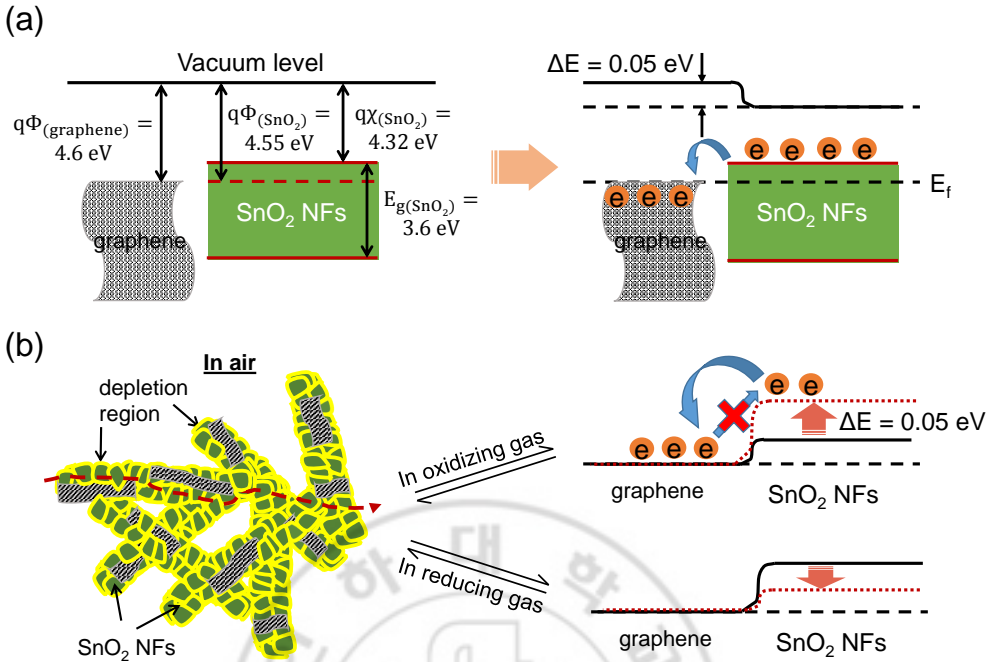
FIGURE 2.7: Sensing mechanism of graphene-loaded SnO$_2$ composite nanofibers

SnO$_2$ and graphene are 4.55 and 4.60 eV, respectively [89–91], with the Fermi energy of SnO$_2$ being lower than that of graphene. Upon the generation of graphene/SnO$_2$ heterointerfaces, electrons will flow from SnO$_2$ to graphene, ultimately equilibrating the Fermi level. This charge transfer will form a potential barrier at the heterojunctions, causing the vacuum energy level and the energy band to bend.

As a first possibility, the initial transfer of electrons from SnO$_2$ to graphene will inevitably develop a surface depletion region on the SnO$_2$ surface. With increased initial resistance, the modulation of the same amount of resistance, upon the introduction/removal of a target gas, will lead to higher sensitivity. As a second possibility, the electrical current across the SnO$_2$/graphene interfaces will provide an additional modulation of the resistance. The reducing gases and oxidizing gases will react with adsorbed oxygens, such as O$^-$, providing and removing

electrons, respectively. Accordingly, reducing and oxidizing gases will decrease and increase the height of potential barriers to electrons, respectively.

We surmise that the electrical currents will dominantly flow through the SnO$_2$ grains. However, it is possible that some electrical current will flow through the graphene. To realize electrical conduction *via* graphene, electrons are required to penetrate into the graphene, with taking out electrons from graphene being easy. However, the barrier height at heterointerfaces (*i.e*, 0.05 eV) prevents electrons from penetrating into graphene. Upon the introduction of a reducing gas, the surface reactions will donate some electrons to the SnO$_2$ surface, thereby increasing the Fermi level of SnO$_2$. This will decrease the relative energy level between SnO$_2$ and graphene. While the electron flow from SnO$_2$ to graphene is still efficient, the electron transfer from graphene to SnO$_2$ becomes easier, contributing to the decreased resistance of the sensor. Since the reducing gas decreases the resistance of the present sensor, the potential barrier of graphene/SnO$_2$ helps to enhance the sensing behavior.

Although oxidizing gases were not tested in the present work, upon the introduction of an oxidizing gas, some electrons should be removed from the SnO$_2$ surface to decrease the Fermi level of SnO$_2$. Thus, the potential barrier will be elevated at graphene/SnO$_2$ interfaces. Accordingly, although the electron flow of SnO$_2$ to graphene will still be efficient, the electron transfer from graphene to SnO$_2$ will be discontinuous. This ultimately increases the resistance of the sensor, contributing to the enhanced sensing behavior.

In the case of graphene-loaded SnO$_2$ composite nanofibers, we first examine the nature and role of graphene nanosheets in the SnO$_2$ nanofibers. The incorporation of graphene leads to an increase in the baseline resistance of the pristine SnO$_2$ nanofibers. The maximum resistance was obtained by using the optimal amount of graphene (0.5 wt%). This indicates the *p*-type or electron accepting nature of the graphene in SnO$_2$ nanofibers. It also shows that the

current flows mainly through interconnected SnO$_2$ nanofibers. This observation is consistent with the previous reports [81, 92]. From this, we can also understand the bell-shaped response behavior of graphene-loaded SnO$_2$ composite nanofibers (Figure 2.4c).

In the case of low to moderate graphene loadings (0.05-0.5 wt%), conductive graphene nanosheets disperse into the nanofibers and active interfaces between graphene and SnO$_2$ are formed. This increases the sensor resistance and the heights of potential barriers. When a reducing gas is introduced, the trapped electrons from the oxygen are released back into the SnO$_2$ nanofibers; thus, a significant change in the resistance is observed. Alternatively, in the case of loading of high concentrations of graphene, it is expected that the overall sensor
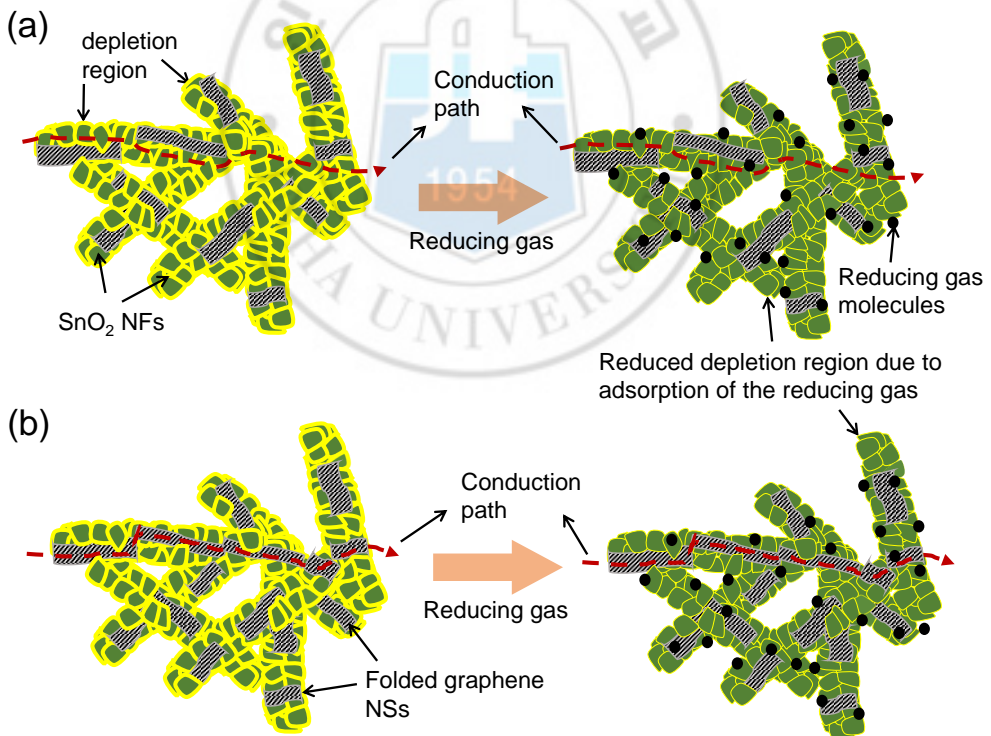
FIGURE 2.8: Schematic of the electrical conduction through (a) SnO$_2$ grains and (b) graphene nanosheets

performance will be reduced (Figure 2.8). First, since electrical conduction mainly occurs through the SnO$_2$ grains, increasing the graphene content may block electrical currents through SnO$_2$ grains, leading to an increase in the initial resistance. However, this will increase the sensor response (defined as R_a/R_g, where R_a is the original base resistance of the sensor in air and R_g is the stabilized resistance of the sensor in the presence of the applied gas). Since the initial resistance (R_a) is smaller, the same decrease in resistance caused by the introduction of a reducing gas yields a higher R_a/R_g value. Accordingly, this cannot account for the observed decrease in the sensor response that is caused by increasing the graphene content.

Secondly, when a sufficient amount of graphene is provided, graphene nanosheets begin to connect with each other to provide additional pathways for the flow of electrons (Figure 2.8b). In this case, the flow of electrons occurs mainly through higher conducting pathways along graphene nanosheets. This will decrease the initial resistance; the same decrease in the resistance caused by the introduction of a reducing gas yields a lower R_a/R_g value, thereby reducing the sensor response.

This type of behavior has been reported elsewhere as a function of the graphene concentration [81]. In fact, such behavior has been widely observed when a metal oxide is sensitized by a catalyst or an additive [68, 93]. Therefore, there should be an optimal loading amount of graphene that achieves high sensing performance in SnO$_2$ nanofibers; this value was around 0.5 wt% in these experiments. This optimal amount of graphene may seem too small to cause a significant change but the actual volume and number of graphene nanosheets incorporated are very large due to the very small density of graphene. Thus, there are a large number of graphene/SnO$_2$ heterointerfaces, which cause a significant effect on the resistance modulation of SnO$_2$ nanofibers.

In the present work, it is revealed that our optimized graphene-loaded SnO$_2$

composite nanofibers have great potential to be used as low concentration gas sensors. Although we provided many possible reasons to explain the enhanced sensitivity of the graphene-loaded SnO$_2$ composite nanofibers (as compared to pristine SnO$_2$ nanofibers), further comprehensive studies investigating the gas-surface interactions are required to explain some of the peculiar observations, including the improved H$_2$S sensing properties. The improved response and rapid response time for H$_2$S can be ascribed to the enhanced surface reaction that is caused by the increased surface area, which facilitates more gas adsorption and diffusion. The average bond energies for H-S (in H$_2$S), C-H (in benzene), and C-O (in CO) are 347.3 kJmol^{-1}, 414.2 kJmol^{-1}, and 359.8 kJmol^{-1}, respectively [94]. Since the sensing reactions will be enhanced by the effective decomposition of the target gas, the lower average bond energy (*i.e*, higher reactivity) of H$_2$S also suggests its rapid detection and interaction with the nanosized network of graphene-loaded SnO$_2$ composite nanofibers; this is consistent with the current results ($\tau_{res} = 3.2$ s at 5 ppm of H$_2$S).

2.4 Summary

In this chapter, we compared the gas sensing characteristics of graphene-loaded SnO$_2$ composite and pristine SnO$_2$ nanofibers at very low concentrations of C$_6$H$_6$, C$_7$H$_8$, CO, CO$_2$, and H$_2$S gases at various temperatures ranging from 200 to 400 °C. FE-SEM and HR-TEM analyses confirmed the presence of graphene nanosheets and revealed the nature of their interaction with the nanograins of the polycrystalline nanofibers. The optimal amount of graphene and the optimum operating temperature were observed to be 0.5 wt% and 300 °C, respectively. The loading of graphene nanosheets into SnO$_2$ nanofibers not only enhanced the sensitivity but also lowered the optimal operating temperature of the SnO$_2$ nanofibers. The optimized graphene-loaded SnO$_2$ composite nanofibers exhibited

sensor responses of 6.46 and 11.6 at 1 and 5 ppm of H$_2$S gas, respectively. They also showed an extremely short response time of 3.2 s at 5 ppm of H$_2$S gas. Apart from the modulated resistance along the surface and in the grain boundaries of the nanograins in the SnO$_2$ nanofibers, the enhanced sensing capabilities caused by the incorporation of graphene nanosheets is ascribed to a variety of mechanisms. These include the catalytic effects of graphene and the generation of SnO$_2$/graphene heterointerfaces. Since graphene-loaded SnO$_2$ composite nanofibers showed excellent sensitivity towards very low concentrations (1-5 ppm) of gases, these graphene-loaded SnO$_2$ composite nanofibers are potential candidates for next-generation gas sensors.
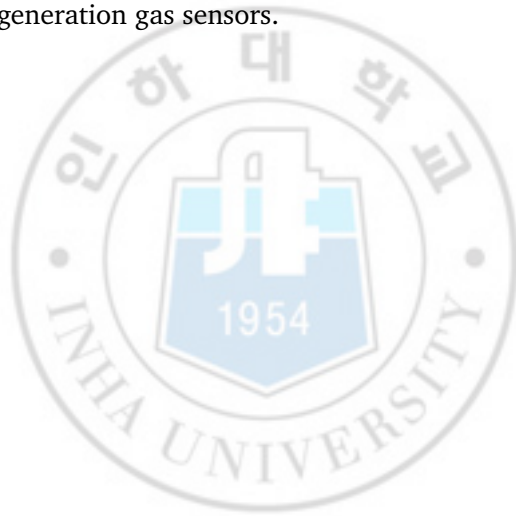
Chapter 3

Reduced Graphene Oxide-loaded ZnO Composite Nanofibers

Herein, the sensing properties of n-ZnO nanofibers doped with reduced graphene oxide (RGO) nanosheets are investigated. Our synthesis utilizes a very simple and cost-effective electrospinning process. The present RGO-loaded ZnO nanofibers contain several characteristics that are favorable for gas sensors. Not only do these sensors utilize the largest grain boundary area provided by the electrospun nanofibers structure, but they also consist of sensing materials (*i.e*, ZnO and RGO) with inherently advantageous characteristics. Furthermore, these sensors create local p-n heterojunctions at the heterointerfaces of ZnO/RGO, achieving the best sensing performance at the optimal amount of RGO for the detection of trace amounts (1, 2, and 5 ppm) of different oxidizing and reducing gases. Detailed characterization of RGO-loaded ZnO nanofibers is carried out to understand the interactions between RGO nanosheets and ZnO nanograins. The sensing characteristics are examined as a function of the concentration of RGO nanosheets. Experimental results indicate that the addition of RGO and the creation of local p-n heterojunctions greatly improve the sensing characteristics of the ZnO nanofibers.

Finally, in the end of the chapter, we propose a novel hybrid sensing mechanism for the drastic improvement in the sensing behavior that is caused by loading RGO nanosheets into ZnO nanofibers. This hybrid sensing mechanism combines the resistance modulation of ZnO/ZnO homointerfaces and RGO/ZnO heterointerfaces in addition to the radial modulation of the surface depletion layer of ZnO nanofibers. In the heterointerfaces, the creation of local heterojunctions plays a significant role in raising the sensitivity of RGO-loaded ZnO nanofibers. This is a promising method to fabricate practical sensors with high sensing capabilities. In this regard,we explain the novel hybrid sensing mechanism of these composite nanofibers, which enables their exceptionally high response to all gases. The presented synthesis procedure, which is both simple and cost-effective, is beneficial for the practical fabrication of these detectors.

3.1 Introduction

The sensing ability of materials can be greatly increased by reducing their size down to the nanometer scale, presumably through the preparation of nanodots, nanowires, nanofibers, and nanowebs [95]. However, nanofibers, which are one-dimensional nanostructures comprised of many nanograins, have been identified as the most promising structure for the successful detection of analytes (even when the concentration is as low as ppb) among the various types of nanostructures [96]. The extraordinary sensing properties of nanofibers are primarily ascribed to their large surface to volume ratio as compared to other nanostructures. Due to the fact that they contain many small grains, nanofibers possess large grain boundary areas. Consequently, a larger amount of analytes can diffuse along the boundaries, resulting in enhanced sensitivity.

Many synthesis procedures for nanofibers have been investigated over the last few decades, but electrospun nanofibers are dominant in chemical sensor

applications because the processing parameters and the characteristics (*e.g*, morphology, diameter, aspect ratio, nature of the nanofibers, *etc*) of the nanofibers can be easily controlled; these variables heavily influence the chemical sensing abilities. In addition, the electrospinning method is incredibly effective for low-cost mass production with the minimal usage of materials, which makes it the most suitable method for industrial applications on the commercial scale. For these reasons, electrospun nanofibers have been employed in a diverse range of sensing materials [97–103].

Possessing a wide bandgap (3.37 eV) with a large exciton energy (60 meV) [104], ZnO nanofibers-based semiconductors are one of the most promising sensing materials and have been extensively studied for the past several years [105–107]. However, despite their inherent advantageous characteristics, there is still room for improvement. Because ZnO based sensors are usually good for high temperature environments, they oftentimes require more power, which affects their long term stability. Further enhancement of their sensing performance is strongly required.

In order to efficiently improve the sensitivity of nanostructured gas sensors, researchers are currently pursuing synergistic effects between different nanomaterials. Recently, the use of dopants (including Au [108], Ag [109], Pt [110], and Pd [111]) and the creation of local *p-n* heterojunctions in *n*-type ZnO (by mixing with *p*-type semiconductors such as $BaTiO_3$-CuO-La_2O_3 [112], CuO [113], and graphene [114]) have significantly improved the sensing performance of ZnO based gas sensors.

Additionally, chemically derived graphene is expected to be a highly sensitive chemical sensor because of its very high electron mobility [115, 116]. Since it is an exceptionally low-noise material, graphene sensors should be able to detect individual gas molecules and are expected to exhibit an excellent sensing behavior [71]. However, pure graphene faces difficulties in being employed as a practical

sensor because its adsorption of gas molecules is inefficient. In this regard, reduced graphene oxide, which is graphene decorated with oxygen functional groups that provide an increased amount of adsorption sites, is more beneficial for improving sensitivity [117]. A recent study found that highly dispersed ZnO nanoparticles on a graphene surface showed higher sensitivity toward 1000 ppm of acetylene gas [118].

However, for practical applications, more efficient sensors that can effectively detect very small traces of gases are required. Furthermore, properly optimizing the quantity of the RGO is crucial in order to obtain the best sensing performance for small traces of gases that also avoids overloading of the dopant and minimizes the cost. To the best of the authors' knowledge, no attempts have been reported regarding the creation of local heterojunctions in n-ZnO nanofibers with RGO nanosheets.

3.2   Experimental Details

3.2.1   Materials

Zinc acetate ($(CH_3CO)_2Zn$, Sigma Aldrich Corp.), reduced graphene oxide, and polyvinyl alcohol (PVA, Mw 80,000, Sigma Aldrich Corp.) were used as-received without any further processing or refining. The preparation process of RGO solution is described in detail in a previous report [75].

3.2.2   Synthesis of nanofibers and Sensing Device Fabrication

The procedure to synthesize RGO-loaded ZnO nanofibers is as follows: first, an aqueous solution of PVA (10 wt%) was prepared, in which PVA was dissolved in distilled water. After 4 h of continuous stirring at 65-70 °C, the zinc acetate and RGO solution was added to the PVA solution, subsequently being stirred for an

additional 6 h at 70 °C. Since TEM investigation of RGO-loaded ZnO nanofibers does not clearly show the individual image of RGO nanosheests, we estimated the sizes of RGO nanosheets in source materials, from many TEM images. The average size was measured to be about 75 nm, which is smaller than the diameter of ZnO nanofibers.

Next, this viscous solution was used to produce RGO-loaded ZnO nanofibers by a conventional electrospinning method; the prepared viscous solution was loaded into a syringe equipped with a 21-guage stainless steel needle with an inner diameter of 0.51 mm. Applied voltage, feed rate, and distance between the collector and the needle tip were set to 15 kV, 0.03 mL/h, and 20 cm, respectively. The voltage was applied to the needle tip, whereas the metal collector was grounded. The nanofibers were deposited onto SiO_2 substrates, with a uniform distribution, as described in our previous reports [104, 119] and shown in Figure 3.1a. All of the electrospinning experiments were done at room temperature. Calcination of the nanofibers was carried out in air for 5 h at 500 °C with a heating rate of 0.5 °C/min, to remove the polymer solvents. In total, six sensor devices were fabricated to investigate ZnO nanofibers containing different quantities of RGO nanosheets (0.04, 0.11, 0.17, 0.44, 0.77, and 1.04 wt%). Since RGO is known to be stable at temperatures in the range of -10 to 800 °C [120, 121], the RGO nanosheet will not be decomposed during the calcination process at 500 °C. Subsequently, for gas sensing measurements, Ti (thickness: $\sim$ 50 nm) and Pt (thickness: $\sim$ 200 nm) were deposited on the substrates via magnetron sputtering using interdigitated electrodes.

3.2.3 Characterization and Sensing Measurements

The microstructural and morphological characteristics of RGO-loaded ZnO nanofibers were investigated by field-emission scanning electron microscopy (FE-SEM, Hitachi S-4200) and transmission electron microscopy (TEM, Phillips
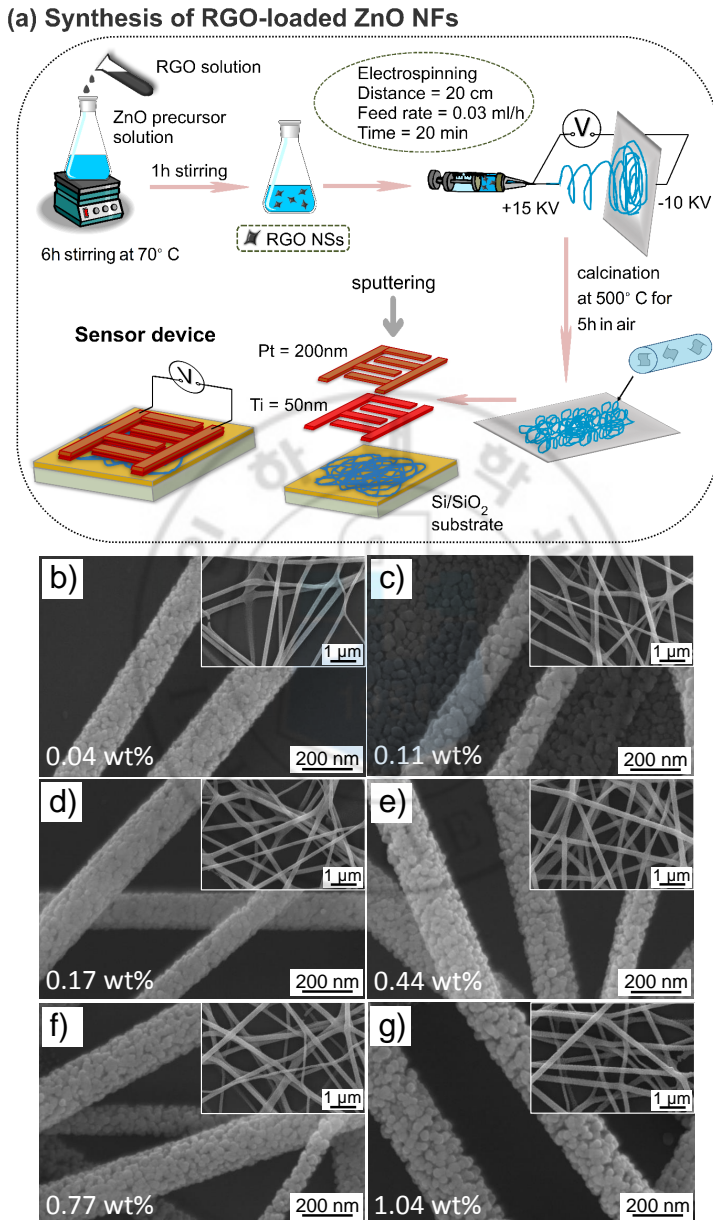
FIGURE 3.1: (a) Schematic of the synthesis and (b) SEM of RGO-loaded ZnO nanofibers

CM-200). The structural phase analysis was carried out using X-ray diffraction (XRD, Phillips X'pert MRD). For SEM, the samples were cleaned by several steps, including ultrasonic cleaning, blow-drying, and drying using oven or hotplate. They were sputter-coated with Pt layer, in order to eliminate the charge effect. For TEM, the samples were dispersed in acetone ultrasonically. Subsequently, drops of the suspension were located on the amorphous carbon films supported on copper grids. The sample-comprising grids were dried in air.

Raman spectra were acquired at room temperature with a Raman microscope (LabRam HR800 UV; Horiba Jobin-Yvon, France) at Korea Basic Science Institute (KBSI). The excitation light source was a diode laser with a wavelength of 514 nm. The laser power incident on the sample surface was 10% of 10 mW. The D and G peaks of graphite, being originated from surface RGOs, were observed, in addition to ZnO-related ones.

In order to fabricate the sensor device, we have sputter-deposited Pt ($\sim$ 200 nm) and Ti ($\sim$ 50 nm) sequentially, on the specimens by means of using an interdigital electrode mask. The I-V test showed pseudo-ohmic characteristics. The sensing performance of RGO-loaded ZnO nanofibers was investigated for common oxidizing (NO_2, SO_2, and O_2) and reducing (CO, C_6H_6 (benzene), and C_2H_5OH (ethanol)) gases using a custom made gas-sensing system. The gas sensing measurements were carried out at three different temperatures (300 °C, 350 °C, and 400 °C), which were optimized in our previous reports [119, 122]. The gas concentration was controlled using accurate mass flow controllers. For oxidizing gases, the gas response was calculated by R_g/R_a, where R_g is the impedance of the sensor in the applied target gas and R_a is the resistance in the air or in the absence of the target gas. For reducing gases, the gas response was determined to be R_a/R_g.
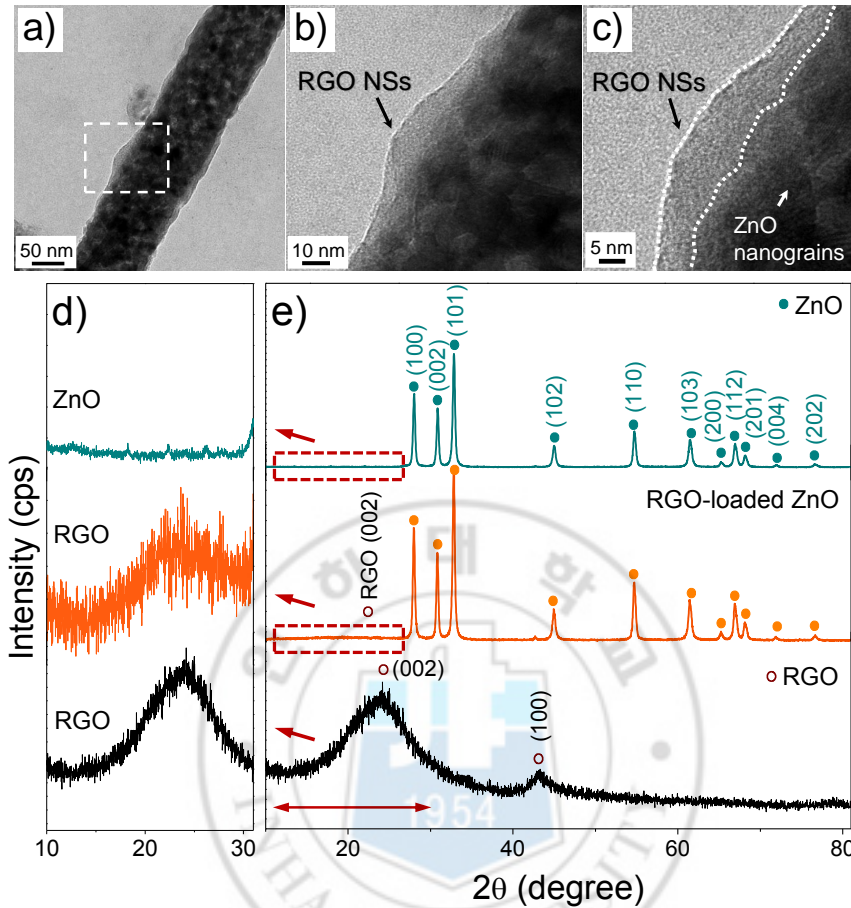
FIGURE 3.2: (a)-(c) TEM of RGO-loaded ZnO nanofibers (d)-(e) XRD patterns of ZnO, RGO-loaded ZnO nanofibers and RGO nanosheets

3.3   Results and Discussion

3.3.1   Microstructural Anaylsis

The microstructures of the synthesized RGO-loaded ZnO nanofibers are shown in Figure 3.1b-g. The average diameter of the calcined nanofibers is measured to be about 150 nm. Because the sensing properties of oxide-based semiconductor gas sensors are greatly affected by the size of their nanograins, SEM images of RGO-loaded ZnO nanofibers were taken. These images clearly exhibit the

existence of nanograins. Figure 3.1b-g reveals that the size of the nanograins and/or the diameter of the nanofibers were not influenced as the amount of RGO nanosheets was changed. The upper-right insets reveal that the nanofibers are uniformly distributed on the substrates.

In order to investigate the configuration of RGO nanosheets and their interactions with ZnO nanograins, we carried out a TEM analysis. Figure 3.2a shows a low-magnification TEM image of an RGO-loaded ZnO nanofiber. Figure 3.2b is a magnified TEM image that shows an enlarged image of the dotted square in Figure 3.2a. In Figure 3.2c, the RGO nanosheet can be clearly observed. Also, the presence of nanograins in the TEM images indicates the polycrystalline nature of the ZnO. RGO nanosheets have been attached to the boundaries of the nanograins, likely creating localalized heterojunctions with the n-type ZnO nanograins. The phase analysis of the synthesized nanofibers was performed by XRD and supports the presence of RGO nanosheets in ZnO nanofibers, as shown in Figure 3.2d-e. Figure 3.2e shows the representative XRD patterns of monolithic ZnO nanofibers, RGO-loaded ZnO nanofibers, and pure RGO nanosheets, respectively. All of the peaks of RGO-loaded ZnO nanofibers agree well with those of monolithic ZnO nanofibers (JCPDS Card No. 891397). However, a broad diffraction peak (d-spacing 3.7 Å at $2\theta = 24.0°$) of RGO nanosheets was also observed in RGO-loaded ZnO nanofibers, as clearly depicted in Figure 3.2d. This broad diffraction peak of RGO is very close to the typical (002) diffraction peak of graphite (d-spacing 3.35 Å at $2\theta = 26.6°$) [115, 123]. From these results, TEM and XRD analyses both confirm the presence of RGO nanosheets in RGO-loaded ZnO nanofibers.

3.3.2 Sensing Results

The sensing properties of these RGO-loaded ZnO nanofibers were evaluated by exposing them to different oxidizing (NO_2, SO_2, and O_2)and reducing (CO, C_6H_6,

a)

b)
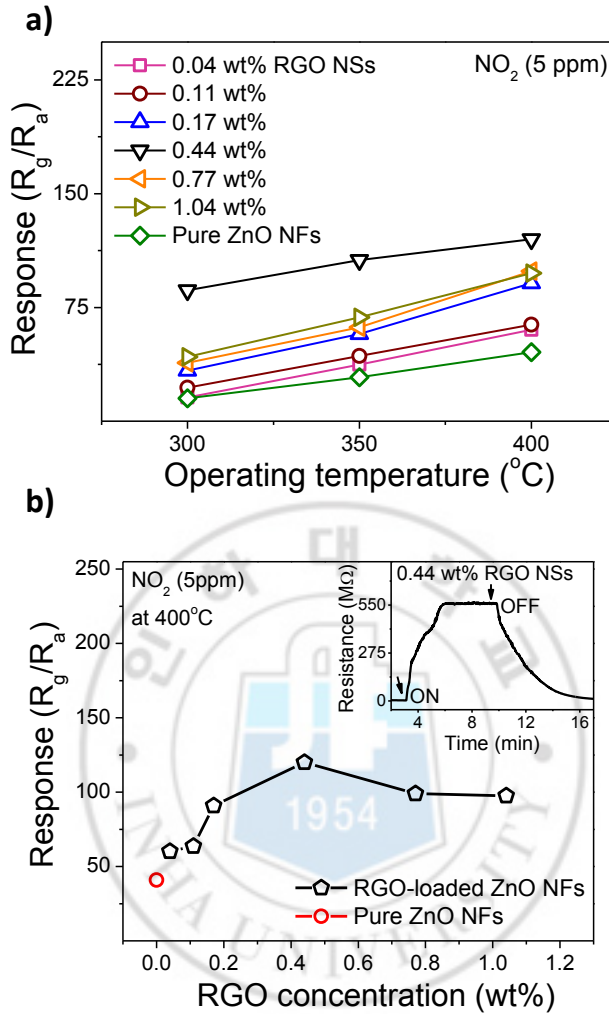
FIGURE 3.3: (a) Responses of all sensors to NO_2 as a function of temperature and (b) as a function of RGO concentration (wt%) at 400 °C

and C_2H_5OH) gases between 300 and 400 °C. The concentrations of the gases were set to 1, 2, and 5 ppm.

Figure 3.3a summarizes the sensor responses as the weight percent of the RGO was varied between 0 and 1.04 wt%. The NO_2 concentration was set to 5 ppm and the sensing temperature ranged from 300 to 400 °C. Each sensor clearly showed an increase in resistance with the introduction of NO_2 gas. Upon the removal

or stoppage of the gas, the sensors again showed a decrease in their resistivity. This trend of changing resistance can be defined in terms of the framework of n-type semiconductors, in which the major charge carriers are electrons. NO_2 gas molecules adsorb onto the surfaces of the nanofibers, diffuse and take electrons from the nanofibers, and then create electron depleted regions, eventually leading to the decrease in the conductivity of the nanofibers. Likewise, emission of electrons occurs when the NO_2 gas is removed. However, the transfer of electrons and the formation of anions (here NO_x^- or oxygen anions in the presence of oxygen) on the surface of the sensing material are significantly dependent on the temperature and sensing material. All sensors containing RGO nanosheets showed a higher response than pure ZnO nanofibers at all temperatures. It is noteworthy that the best response was achieved at 400 °C. Figure 3.3b shows the variation of sensor responses as the weight percent of the RGO was varied between 0 and 1.04 wt% at an NO_2 concentration and temperature of 5 ppm and 400 °C, respectively. The sensor containing 0.44 wt% RGO nanosheets showed a higher response than the other sensors at all temperatures (Figure 3.3a). The sensor response decreased once the amount of RGO nanosheets increased above 0.44 wt%, indicating that the amount of RGO nanosheets must be optimized in order to achieve the best sensing properties. The upper-right inset in Figure 3.3b demonstrates the typical change in resistance of the sensors upon the supply and stoppage of NO_2 gas.

In order to further investigate the sensing properties, the responses of the sensors were measured against other oxidizing gases, such as SO_2 and O_2, at 400 °C. The dynamic sensing curves of oxidizing gases are shown in Figure 3.4a. The data for the sensing responses are summarized in Figure 3.4b. The responses to SO_2 and O_2 were significantly lower than the response to NO_2, which is mainly due to the higher reactivity of NO_2 gas molecules to general sensing materials as compared to SO_2 and O_2. For comparison, the responses of pure ZnO nanofibers to the oxidizing gases are shown in Figure 3.4c. Figure 3.4b-c clearly reveal that
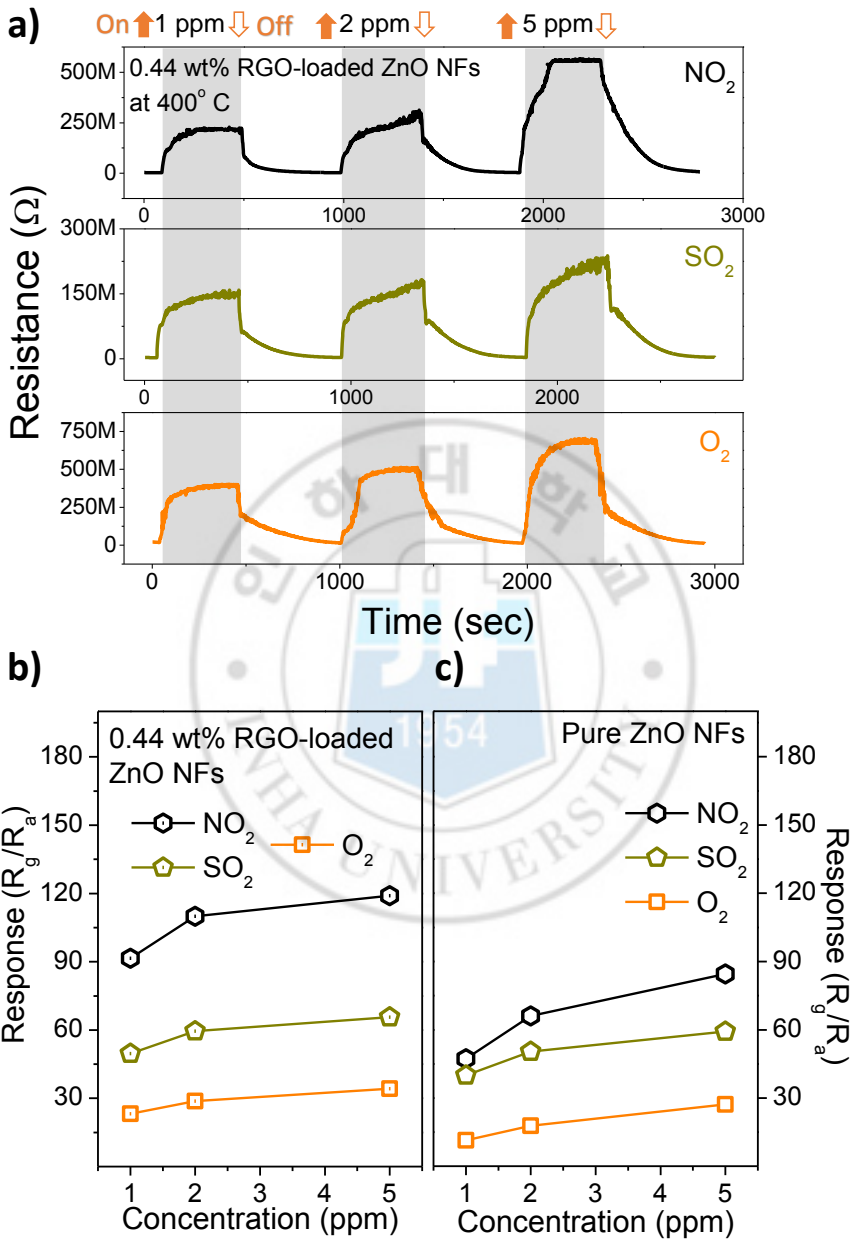
FIGURE 3.4: (a) The resistance curves and (b) responses of 0.44 wt% RGO-loaded ZnO nanofibers for oxidizing gases

the loading of RGO nanosheets into ZnO nanofibers significantly enhances the sensitivity of the ZnO nanofibers. Close examination reveals that the incorporation of RGO nanosheets significantly enhanced the sensing response to NO_2 gas.

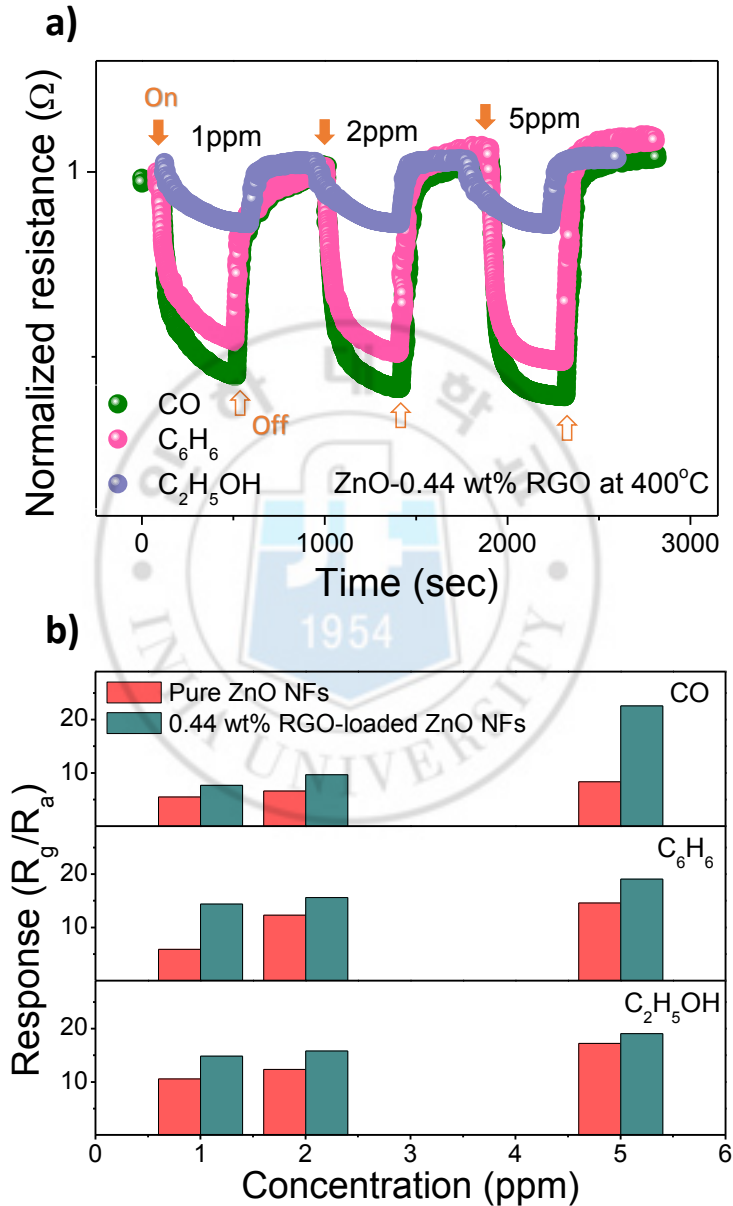**FIGURE 3.5:** (a) The resistance curves of 0.44 wt% RGO-loaded ZnO nanofibers for reducing gases and (b) comparison of the responses with pure ZnO nanofibers

The sensor containing 0.44 wt% RGO nanosheets was further examined with different reducing gases (CO, C_6H_6, and C_2H_5OH). These dynamic sensing curves are shown in Figure 3.5a, exhibiting typical n-type behavior. Upon introduction of the reducing gases, the resistivity of the sensors decreased and then again increased to the maximum level upon the removal of the gas. The sensing behavior of n-type semiconductors toward reducing analytes is exactly opposite to that of the oxidizing analytes and can be defined by the reduction-reoxidation mechanism [95]. The reducing gases react and partially reduce the oxide surface, leading to an increase in the number of free electrons in the conduction band (*i.e*, a reduced resistivity). Reoxidation of the surface occurs upon desorption or removal of the reducing analyte, leading to an increase in the conductivity. The responses of the reducing gases (and the results of pure ZnO nanofibers) are summarized in Figure 3.5b as a function of gas concentration. Again, the responses of RGO-loaded ZnO nanofibers were superior relative to the pure ZnO nanofibers, clearly demonstrating the effectiveness of the RGO nanosheets. This improved performance maybe caused by the formation of local heterojunctions at the RGO/ZnO interfaces.
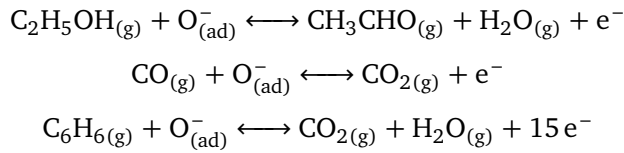
3.3.3 Sensing Mechanism

In order to explain the operation of the sensing mechanisms in RGO-loaded ZnO nanofibers that leads to their exceptionally high sensitivity, several mechanisms must be considered. First, there is the modulation of the resistance along the surface of the ZnO nanofibers. In air ambient conditions, oxygen molecules adsorb, diffuse, and trap electrons from the surface of ZnO nanofibers to form atomic and molecular ions (O^-, O^{2-}, and O_2^-) [124]. An electron-depleted region is established within the Debye length underneath the surface due to the extraction of electrons by these adsorbed ions. The width of the depleted region increases or decreases as the chemisorbed oxygen reacts with the oxidizing or
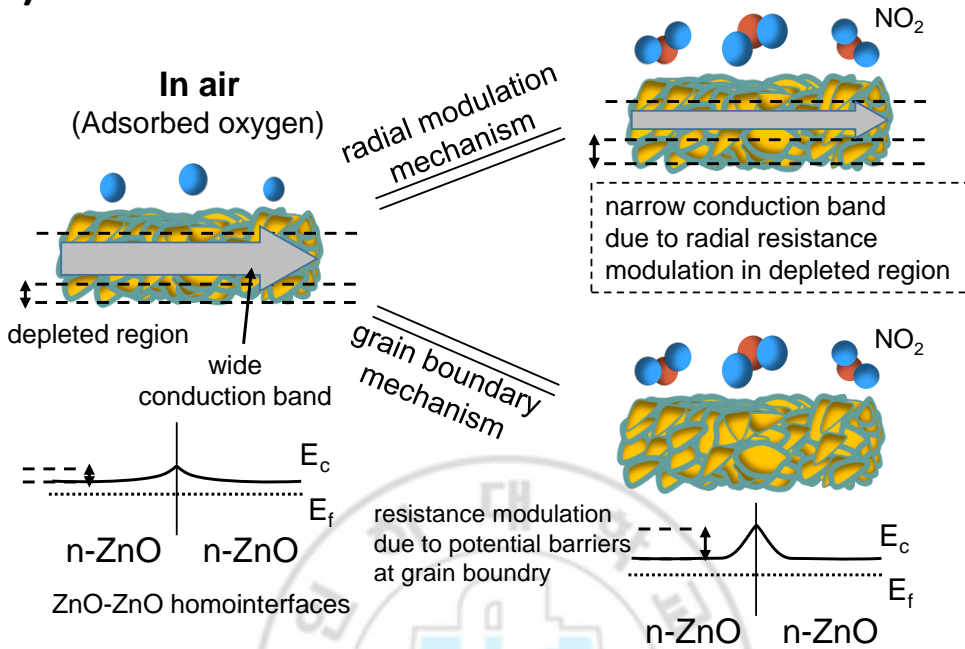
reducing analytes, respectively.

For example, the interaction of reducing analytes ($e.g$, C_2H_5OH, CO, and C_6H_6) has been proposed in the literature [95, 122] as follows:

$$C_2H_5OH_{(g)} + O_{(ad)}^- \longleftrightarrow CH_3CHO_{(g)} + H_2O_{(g)} + e^-$$

$$CO_{(g)} + O_{(ad)}^- \longleftrightarrow CO_{2(g)} + e^-$$

$$C_6H_{6(g)} + O_{(ad)}^- \longleftrightarrow CO_{2(g)} + H_2O_{(g)} + 15\,e^-$$

Second, we will explain the sensing mechanism of monolithic ZnO nanofibers, in regard to the ZnO/ZnO homointerfaces (Figure 3.6a).   The gas sensing properties of nanofibers are mainly related to the presence of nanograins in the polycrystalline sensing materials. The boundaries between these nanograins act as potential barriers to the flow of electrons. In air ambient, the adsorbed oxygen (such as O^-) will be present at the grain boundaries of ZnO. The adsorbed species extract electrons by the reactions such as the following [125]: $2\,O^- + V_0^{+2} + 2\,e^- \longleftrightarrow O_0$. Accordingly, the potential barrier to the flow of electrons will appear at the boundaries. Upon the introduction of oxidizing and reducing gases, the potential barrier will become higher and lower, respectively, thereby increasing and decreasing the resistance across the grain boundaries along the ZnO nanofibers. The sensing enhancement with the ZnO/ZnO homointerfaces can also be explained by the evolution of the depletion layer along the grain boundaries. The resistance modulation arises from nanograin boundaries, by the expansion or suppression of the depletion layer.

Third, the RGO nanosheets-loaded ZnO nanofibers offer additional sources for sensor enhancement, being compared to the pure ZnO nanofibers. We will explain the sensing mechanism, with respect to the ZnO/RGO heterointerfaces (Figure 3.6b). With a large amount of RGO nanosheets being distributed in the ZnO nanofibers, no direct contact will take place between the neighboring RGO nanosheets. Since the adjacent nanosheets are not physically connected,

a) Pure n-ZnO NFs

In air
(Adsorbed oxygen)

radial modulation mechanism

NO$_2$

narrow conduction band
due to radial resistance
modulation in depleted region

depleted region

wide conduction band

grain boundary mechanism

E$_c$

E$_f$

n-ZnO   n-ZnO

ZnO-ZnO homointerfaces

resistance modulation
due to potential barriers
at grain boundry

NO$_2$

E$_c$

E$_f$

n-ZnO   n-ZnO

b) p-RGO-n-ZnO heterojunctions

In air
(Adsorbed oxygen)

In oxidizing gas

NO$_2$

E$_c$

E$_f$

p-RGO   n-ZnO

In reducing gas

E$_c$

E$_f$

p-RGO   n-ZnO

CO

E$_c$

E$_f$

p-RGO   n-ZnO

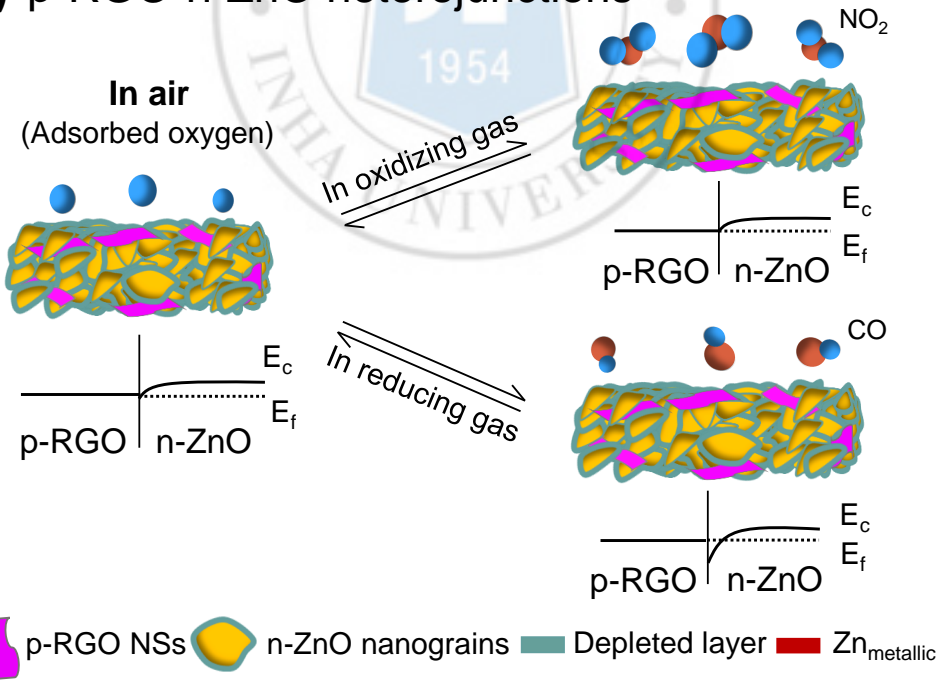p-RGO NSs   n-ZnO nanograins   Depleted layer   Zn$_{metallic}$

FIGURE 3.6: Sensing mechanism of (a) pure *n*-ZnO nanofibers and (b) RGO-ZnO heterojunctions

52

the electrical conduction in the sensor devices will mainly occur through the ZnO nanofibers, rather than discretely distributed RGO nanosheets. Figure 3.6b indicates that a considerable amount of local heterojunctions (*i.e,* ZnO/RGO composite system) exists in RGO-loaded ZnO nanofibers.

It is possible that the ZnO/RGO interfaces as well as ZnO grain boundaries will contribute to the enhancement of sensing behavior. In the heterojunctions, the Fermi energy of ZnO is supposed to be lower than that of RGO, with the work functions of *n*-ZnO and RGO being about 5.20 and 4.75 eV, respectively (Figure 3.6b). The RGO will be regarded as a kind of metal-like material. In order to equate the Fermi level, electrons will be transferred from RGO to *n*-ZnO. Resulting from the charge transfer, the potential barrier will be formed at heterojunctions, with the bending of the vacuum energy level and the energy band. In the present case, in which the work function of the metal is lower than that of the *n*-type semiconductor, the ohmic contact will be generated, becoming a non-rectifying barrier to the flow of electrons. In spite of the non-rectifying nature,the established potential barrier will affect the sensing behavior.

As a first possibility, the enlarged surface depletion region of ZnO nanofibers will enhance the sensing behavior. Since ZnO becomes more *n*-type than the original state, the energy barrier between ambient gas and ZnO will be further reduced [126, 127], presumably enlarging the surface depletion region and thus reducing the conduction region simultaneously. With the increased initial resistance, the modulation of resistance by the sensing target gas will turn out to be a higher sensitivity.

As a second possibility, the electrical current across the ZnO/RGO interfaces will provide additional modulation of resistance. In air ambient, the adsorbed oxygen will be present not only at the grain boundaries of ZnO, but also at the ZnO/RGO interfaces. The reducing gases will react with adsorbed oxygen such as O^-, providing electrons. The oxidizing gases will react with the adsorbed oxygen

or provide the adsorbed oxygen, ultimately taking out electrons. The reducing and oxidizing gases will decrease and increase the height of the potential barriers to the electrons, respectively. In air ambient, the electron will easily flow from ZnO to RGO, because there is no potential barrier from ZnO to RGO (Figure 3.6b). For electrical conduction through the sensor devices in terms of RGO nanosheets, the electrons, which were penetrated into the RGO, need to be taken out of the RGO nanosheets. However, the barrier height at the heterointerfaces (*i.e*, 4.5 eV) will prevent the electrons from escaping to the outer ZnO grains.

Upon the introduction of oxidizing gas, the potential barrier will be enhanced at the n-ZnO/RGO interfaces, increasing the relative energy level of n-ZnO to RGO. Accordingly, the electron flow of RGO to n-ZnO will become much more difficult, ultimately increasing the resistance of the sensor. On the other hand, upon the introduction of reducing gas, the energy level of n-ZnO will be suppressed, reducing the relative energy level of n-ZnO to RGO. Accordingly, the electron flow of p-RGO to n-ZnO will become easier, ultimately decreasing the resistance of the sensor.

As a third possibility, discretely distributed RGO nanosheets, which are nanostructures with a higher surface accessibility, will exert the spillover effect, playing a catalytic role in adsorption, dissociation, and transportation (to neighboring ZnO surface) of NO_2 gas molecules. A lot of defects and functional groups on the RGO surface will provide adsorption sites for the gas molecules and will increase the sensitivity.

Although graphene oxide (GO) contains saturated sp^3 carbon atoms bound to oxygen, which makes it an insulator, RGO still contains residual oxygen that is sp^3 bonded to the carbon atoms [128]. It is commonly accepted that the thermal annealing of GO or RGO will reduce the oxygen functional groups. Accordingly, by the heating at 350-400 °C during the sensing tests, it is expected that the RGO embedded in ZnO nanofibers will be further reduced by losing oxygen. Since the

currents in the sensing device mainly flow through continuous ZnO, the surface of RGOs, which is exposed to ambient, will play a catalytic role only.

Due to the resistance modulation caused by these sources, RGO-loaded n-ZnO nanofibers showed a larger change in their resistance compared to monolithic ZnO nanofibers. The resistance of the sensors increased upon the addition of RGO and reached a maximum at 0.44 wt%. At higher concentrations of RGO nanosheets, the resistance decreased. After this critical value, further additions of RGO nanosheets had no substantial effect on the resistance change of the sensors. However, at this time, we cannot explain why further loading of RGO nanosheets (above 0.44 wt%) unexpectedly decreases the sensing behavior. An additional systematic study is currently underway to describe this phenomenon in a following report.

Accordingly, we suggest that the combination of two sensing mechanisms, being related to ZnO/ZnO homointerfaces and RGO/ZnO heterointerfaces, is responsible for the enhancement of the sensing capabilities of RGO-loaded ZnO nanofibers. Thus, we can safely conclude that this hybrid sensing mechanism, which combines the effects of radial resistance modulation, ZnO/ZnO grain boundary modulation, and local p-n heterojunctions (due to the presence of RGO nanosheets), is primarily responsible for the enhancement of the sensitivityof n-ZnO nanofibers.

Although the present sensor is comprised of RGO, this work focused mainly on the ZnO nanofibers sensors, because main conduction occurs through the continuous ZnO nanofibers, rather than discrete RGO nanosheets. The role of RGO nanosheets in enhancing the sensitivity is mainly related to the generation of ZnO/RGO heterojunctions and in addition, discrete RGO nanosheets will exert the spillover effect, playing a catalytic role in adsorption, dissociation, and transportation (to neighboring ZnO surface) of NO_2 gas molecules. Accordingly, direct comparison between the present sensor and RGO or graphene based

TABLE 3.1: Response and recovery times of RGO loaded ZnO composite nanofibers

Gases	Responses time (sec)			Recovery time (sec)		
	1 ppm	2 ppm	5 ppm	1 ppm	2 ppm	5 ppm
NO_2	174	350	143	107	188	259
SO_2	148	297	255	196	231	237
O_2	140	138	153	309	278	270

sensors is meaningless. W. Yuan et al. summarized the sensing capabilities of graphene based gas sensors [117]. Graphene sensor has a particularly different application, from the conventional semiconductor sensors, such as ZnO. Graphene has the lowest resistivity at room temperature among the substances and small amount of extra electrons can cause a noticeable change in the conductance of graphene. Accordingly, it will be suitable for low temperature and extremely low concentration operation. As shown in Table 1 of Ref. [117], the actual sensitivity is relatively low, *i.e*, less than 2. It is noteworthy that the composite materials including graphene will attain the sensor responses higher than 2. For example, highly aligned SnO_2 nanorods on graphene nanosheets exhibited a sensor response of 2.1 for H_2S gas [129]. However, in the present work, we embedded RGO nanosheets into ZnO nanofibers, assigning unusual roles to the RGO nanosheets and attaining the very high sensor response.

From Figures 3.4 and 3.5, we reveal that the sensor responses of RGO-loaded ZnO nanofibers to NO_2, SO_2, O_2, CO, C_6H_6,and C_2H_5OH are 119.0, 65.7, 34.2, 22.6, 19.1, and 19.1, respectively, at a gas concentration of 5 ppm. The RGO-loaded ZnO nanofibers turned out to become an excellent gas sensor for main oxidant and reductive gases. Further techniques including the functionalization will be necessary to enhance the sensor selectivity for a particular gas.

The response times of RGO-loaded ZnO nanofibers to NO_2 gases are 174, 350, and 143 s at 1, 2, and 5 ppm, respectively (Table 3.1). The recovery times of

RGO-loaded ZnO nanofibers to NO_2 gases are 107, 188, and 259 s at 1, 2, and 5 ppm, respectively. The initial resistances of RGO-loaded ZnO nanofibers to NO_2 gases are 3.39, 2.82, and 3.30 MΩ at 1, 2, and 5 ppm, respectively, exhibiting the stable sensing behavior. In addition, the stability of the RGO-loaded ZnO nanofibers was fine; after keeping in air ambient for 2 months, no noticeable sensing difference was observed. After 6 months, the sensor responses to CO gas were decreased by 68.0, 72.1, and 39.8%, respectively, at CO concentrations of 1, 2 and 5 ppm. Further study will be necessary to improve the long-term stability of the present sensor.

3.4 Summary

RGO-loaded ZnO nanofibers were prepared by an electrospinning method. Microstructural investigation revealed that the addition of RGO nanosheets does not affect the size of the ZnO nanograins or nanofibers. Various sensing tests were conducted with a variety of gases, including O_2, SO_2, NO_2, CO, C_6H_6, and C_2H_5OH, which show that our sensors exhibit excellent sensing capabilities. The sensor response to 5 ppm NO_2 gas was increased by the addition of RGO to ZnO nanofibers, reaching a maximum and optimal value of 150 at an RGO concentration of 0.44 wt% at 400 °C. Overall, the RGO-loaded ZnO nanofibers showed higher sensitivity to different oxidizing and reducing gases compared to monolithic ZnO nanofibers. We ascribed this improvement in performance to the hybrid sensing mechanism, which combines the effects of the surface depletion layer of ZnO nanofibers (radial resistance modulation), potential barriers at ZnO grain boundaries (ZnO/ZnO homointerfaces), and RGO/ZnO heterointerfaces. Due to the work function difference of RGO and ZnO, the potential barrier will be generated at the heterointerfaces. This novel hybrid sensing mechanism is responsible for the outstanding sensitivity of RGO-loaded ZnO nanofibers.

Chapter 4

Hydrogen Sensing of Reduced Graphene Oxide-loaded ZnO Composite Nanofibers

Since the detection of hydrogen gas at its very low concentration is crucial not only to ensure safety at hydrogen involving facilities, but also to ensure safe storage and usage of the gas, we have developed a hydrogen gas sensor consisting of RGO-loaded ZnO nanofibers, operating at low concentrations down to 100 ppb. The sensor demonstrated the extremely high response to hydrogen gas at a low concentration. Apart from the existence of nanograin boundaries in the nanofibers, the combined effect of presence of RGO nanosheets and the hydrogen-induced metallization of ZnO semiconductor played a crucial role in enhancing the sensing behavior.

4.1 Introduction

The growing environmental challenges such as air pollution, global warming, and exhaustion of the Earth's resources and the global energy crisis have stimulated considerable research efforts to develop clean, efficient and renewable energy source. Hydrogen is a clean, efficient, and a promising candidate for renewable energy source that will contribute to overcome the problems of global warming, energy supply and security and hence it will be extensively used in power generation and in energy-storage industries. In this emanating hydrogen economy, safety challenges involving hydrogen gas during production, conveyance and storage need highly efficient and sensitive means for early and accurate sensing of escaped or leaked hydrogen gas.

Hydrogen has a very low density (0.0899 kg/m^3) with a high diffusion coefficient (0.61 cm^2/s in air) [130]. Unlike other combustible gases (such as methane, propane *etc*), hydrogen has a low minimum ignition energy (0.017 mJ) and high burning velocity with wide explosive concentration range (4-75%) [131]. Hydrogen is a dangerous gas, becoming explosive and flammable when the concentration is greater than 4% in air [132]. Moreover, because of its colorless, odorless, and tasteless nature, the human senses do not detect H$_2$ gas. Therefore, fast detection of hydrogen gas at its very low concentration is crucial not only to ensure safety at hydrogen involving facilities, but also to ensure safe storage and usage of the gas.

Hydrogen sensors are stable devices that can detect hydrogen molecules and produce an electrical signal. A variety of hydrogen sensor technology has been developed and can be categorized into eight groups based on their sensing mechanisms: chemo-resistive sensors, microelectronics-based sensors, surface acoustic wave sensors, and optical sensors [133]. Among these, chemo-resistive sensors, developed by semiconducting metal oxides (SnO$_2$, ZnO, WO$_3$, TiO$_2$,

etc), have attracted enormous attention and have been extensively studied due
to their low cost and facile synthesis process, stability at higher temperatures
and general higher sensitivity towards various gases. Among various nano-scale
structures of oxide semiconductors, *one-dimensional (1D) electrospun nanofibers*
are distinguishably renowned for potential applications in chemical sensors
mainly due to their large specific area, simple preparation methods, possible
functionalization of their surface with target specific receptor species, and possible
deposit of catalyst over the surface to promote or inhibit specific reactions
[134]. As compared with their thin film counterparts, 1D nanofibers exhibit
higher sensitivity and faster response toward the analyte gas due to their large
surface-to-volume ratio. The electrospun nanofibers, composed of a large number
of nanograins, have a web-like structure, which is completely exposed to the
analyte gas molecules. Moreover, the electrospun nanofibers can be easily
produced on a large commercial scale at low cost, due to the facile electrospinning
process.

Among various metal oxides, Zinc oxide (ZnO) is one of the most common
metal oxides that has been widely employed in chemical sensors because of its
many appealing properties such as good conductivity, low toxicity, good thermal
stability, oxidation resistivity, a direct bandgap (E_g 3.37 eV) with a large exciton
binding energy (60 m eV), and piezoelectricity [133, 135]. More importantly,
previous literature and research show the selectivity of ZnO based gas sensors
towards toxic, flammable and explosive gases, particularly ethanol [136] and
hydrogen [137].

The interaction of hydrogen with ZnO system has been the object of many
studies [138–141] and these studies have led to the conclusion that hydrogen
chemisorption occurring below 100 °C does not affect the conductivity of
ZnO, whereas the chemisorption occurring at high temperatures increases the
conductivity. In order to achieve the highest sensitivity and selectivity in regard

to ZnO, many efforts have been made by means of a variety of strategy, including adding noble metals or oxide catalysts, manipulating the composition and the operating temperature of sensor [142].

The reported RGO based sensors are not highly sensitive and selective to hydrogen gas and to the best of our knowledge, there have been no reports demonstrating the incorporation of RGO in electrospun ZnO nanofibers. Consequently, most of the resistive hydrogen sensors based on graphene that have been reported so far consist of graphene layers functionalized with metal particles. In this contribution, we report a highly sensitive and selective hydrogen sensor fabricated by RGO and ZnO nanofibers by a low-cost and versatile electrospinning process. The RGO-loaded ZnO composite nanofibers showed excellent response with shorter response times and recovery times (depending on concentration and temperature) to a trace concentration of hydrogen gas compared to pristine ZnO nanofibers, pure SnO_2 nanofibers and RGO-loaded SnO_2 composite nanofibers. Sensing results have been characterized as a function of hydrogen concentration and operating temperature. Results show that RGO-loaded ZnO based composite nanofibers can be the promising materials system for the fast and selective detection of hydrogen gas. Furthermore, the easy and facile fabrication process makes them favorable for low cost and large-scale production.

4.2 Experimental Details

4.2.1 Materials

Zinc Acetate $((CH_3CO_2)_2Zn)$, reduced graphene oxide, polyvinyl alcohol (Mw 80,000), tin(II) chloride dihydrate, polyvinylpyrrolidone (Mw 13,00,000), ethanol (anhydrous, 99.5%), dimethylformamide (DMF, anhydrous, 99.8%) were obtained from Sigma Aldrich Corp. and used as received without any further processing or refining.

4.2.2   Preparation of RGO Nanosheets

Graphite powder, H_2SO_4 (98%), H_3PO_4 (98%), $KMnO_4$ (98%) and H_2O_2 (30 wt%), Hydrazine monohydrate (98%), N,N-Dimethylformamide (DMF, 99.8%) were obtained from commercial resources and used as received. GO was synthesized from graphite powder via a modification of Hummers and Offeman's method from graphite powders. In a typical reaction, 5g of graphite, 60 mL of H_3PO_4, and 180 mL of H_2SO_4 were stirred together with a Teflon-coated magnetic stirring in an ice bath. Next, 60 g of $KMnO_4$ was slowly added while the temperature was maintained at 0 °C. Once mixed, the solution is transferred to a 35 ± 5 °C water bath and stirred for 3 h, forming a thick paste. Next, distilled water (450 mL) was slowly dropped into the resulting paste to dilute the mixture, and then the solution was stirred for 1 h while the temperature was raised to 90 ± 5 °C.

Finally, 800 mL of distilled water was added, followed by the slow addition of 60 mL H_2O_2 (30%), turning the color of the solution from dark brown to yellow. During this final step, H_2O_2 (30%) reduced the residual permanganate and manganese dioxide to colorless soluble manganese sulfate. The GO deposit was collected from the GO suspension by high speed centrifugation at 15000 rpm for 30 min. The obtained GO was then washed with 1000 mL of HCl (5%), and repeatedly washed with distilled water until the pH = 7. To obtain uniform GO, a low-speed centrifugation at 3000 rpm was first used to remove thick multilayer sheets until all the visible particles were removed (3-5 min). Then the supernatant was further centrifuged at 10000 rpm for 30 min to remove small GO pieces and water-soluble byproduct.

The final sediment was redispersed in 500 ml of DMF with mild sonication, resulting in a solution of exfoliated GO. In general, for chemically reduced GO (RGO), 500 ml of exfoliated GO was stirred for 30 min, and 10 ml of hydrazine

monohydrate was added. The mixtures were heated at 150 ± 5 °C using an oil bath for 24 h; a black solid recipitated from the reaction mixtures. Products were collected by centrifugation at 12000 rpm for 45 min and washed with DI water and methanol until the pH $= 7$. Next, the obtained RGO was dried and stored in a vacuum oven at 60 °C until use.

4.2.3 Synthesis of RGO-loaded ZnO Composite Nanofibers

The preparation of the precursor solution used to fabricate RGO-loaded ZnO composite nanofibers was prepared by dissolving 10 wt% polyvinyl alcohol in distilled water and the mixture was constantly stirred for 4h at 70 °C. Then, 1 gram of zinc acetate and 0.44 wt% RGO solution was added to the mixture and continuously stirred for 6h at 70 °C.

The precursor solution used to synthesize RGO-loaded SnO_2 was prepared by mixing 8 wt% polyvinylpyrrolidone into a 1:1 solvent mixture of DMF and ethanol and constantly stirred for 4h at room temperature. Then, 1.75 g of $SnCl_2.2H_2O$ and 0.44 wt% RGO solution was added to the mixture and constantly stirred for 12h at room temperature. The amount of RGO loaded in both SnO_2 and ZnO nanofibers was kept constant (0.44 wt%) which was found to be the optimal amount in the previous works [78].

The prepared Zn and Sn precursor solutions were used for electrospinning by loading into syringes with the needles of inner diameter of 0.51 mm. The distance between the tip of the needle and the collector was fixed at 20 cm. The feed rates of the solutions were set to 0.05 mL/h using an accurate syringe pump. The collected as-spun nanofibers, over a Si wafer with 250 nm thick SiO_2 layer, were subsequently heated at 600 °C in the air for 30 min at a heating rate of 0.5 °C/min to remove the polymer solvents. All experiments were performed at room temperature. While the experimental procedures are schematically illustrated in Figure 3.1 in Chapter 3 (see page 42), the details of the processes

used to synthesize the electrospun nanofibers can be found in our earlier reports [104, 137].

4.2.4 Characterization and Sensing Measurements

The morphology and microstructure of the synthesized nanofibers were examined by field-emission scanning electron microscopy (FE-SEM, Hitachi S-4200) and transmission electron microscopy (TEM, Philips CM-200), respectively.

In order to reveal the incorporation of RGO nanosheets, we carried out Raman and XPS analyses. The Raman spectra were acquired using a Jasco laser Raman spectrophotometer NRS-3000 series, with an excitation laser wavelength of 532 nm, at a power density of 2.9 mW.cm^{-2}. XPS was carried out by using a VG Multilab ESCA 2000 system, in which a monochromatized AlKα X-ray source (h$\nu = 1486.6$ eV) was used.

In order to evaluate the sensing properties of the synthesized nanofibers, Ti (thickness: ~ 50 nm) and Pt (thickness: ~ 200 nm) were sequentially deposited on the substrates via magnetron sputtering using interdigital electrodes. A custom-made gas dilution and sensing system were used to measure the responses of the sensors to a range of concentration of hydrogen gas (0.1-10 ppm) at 300, 350 and 400 °C. A known amount of high purity hydrogen gas (>99.999%) was transferred from the storage cylinder to the sensing chamber and the desired amount of concentration was obtained by diluting it with N_2 gas and controlled by using accurate mass flow controllers. The gas response was estimated as (R_a/R_g) by measuring the conductance change of the sensors in the absence and presence of hydrogen, where R_a is the resistance in the absence and R_g is the resistance in the presence of hydrogen. The response and recovery times were calculated by measuring the times needed to reach a 90% change in the resistance on the supply or removal of hydrogen.

4.3   Results and Discussion

4.3.1   Microstructural Analysis

We examined the microstructure and morphology of calcined nanofibers by
field-emission scanning electron microscopy (FE-SEM, Hitachi S-4200) and
high resolution transmission electron microscopy (HR-TEM, Philips CM-200)
(Figure 4.1a-f). After calcination at 600 °C for 30 minutes in the air at a heating
rate of 5 °C/min, the synthesized nanofibers exhibited a regular structure with an
average diameter of 190 nm and composed of a large number of nanograins of
average size 30 nm as shown in Figure 4.1b. The nanofibers and nanograins were
uniform in their size and shape. It is well known that the evolution of nanograins
and their size greatly influence the sensing properties of the nanofibers. The
inset figure is the low-resolution SEM micrograph showing uniform and random
distribution of the composite nanofibers on the Si/SiO_2 substrates.

The presence of nanograins and polycrystalline nature of the composite
nanofibers was also confirmed by TEM examination (Figure 4.1c-d) which was
in good agreement with the SEM micrographs (Figure 4.1a). Figure 4.1e shows
the magnified high-resolution TEM (HR-TEM) image of an enlarged surface
region of an RGO-loaded ZnO composite nanofiber. Several amorphous RGO
nanosheets were observed on the surfaces of the nanograins, likely creating
local heterojunctions with n-ZnO nanograins. The inter-planar distances of ZnO
nanofibers were approximately 0.24 and 0.26 nm, respectively, which correspond
to the (101) and (002) planes of the hexagonal ZnO phase. All the diffraction
ring patterns were indexed to a hexagonal ZnO structure (JCPDS Card No.
89-1397) (Figure 4.1f). The microstructure and morphology of RGO-loaded SnO_2
nanofibers were also investigated by using FE-SEM and HR-TEM and presented in
Figure 4.2.

4.3.2 Sensing Results

In order to characterize the sensing performances of the sensors comprising RGO-loaded ZnO composite nanofibers and RGO-loaded SnO_2 composite nanofibers, we exposed the sensors to a range of hydrogen gas concentration (100 ppb, 1 ppm, 5 ppm and 10 ppm) at various temperatures. Figure 4.3 summarizes the typical dynamic resistance curves while Figure 4.4 shows the sensor responses of RGO-loaded SnO_2 and RGO-loaded ZnO composite nanofibers at 300, 350, 400,
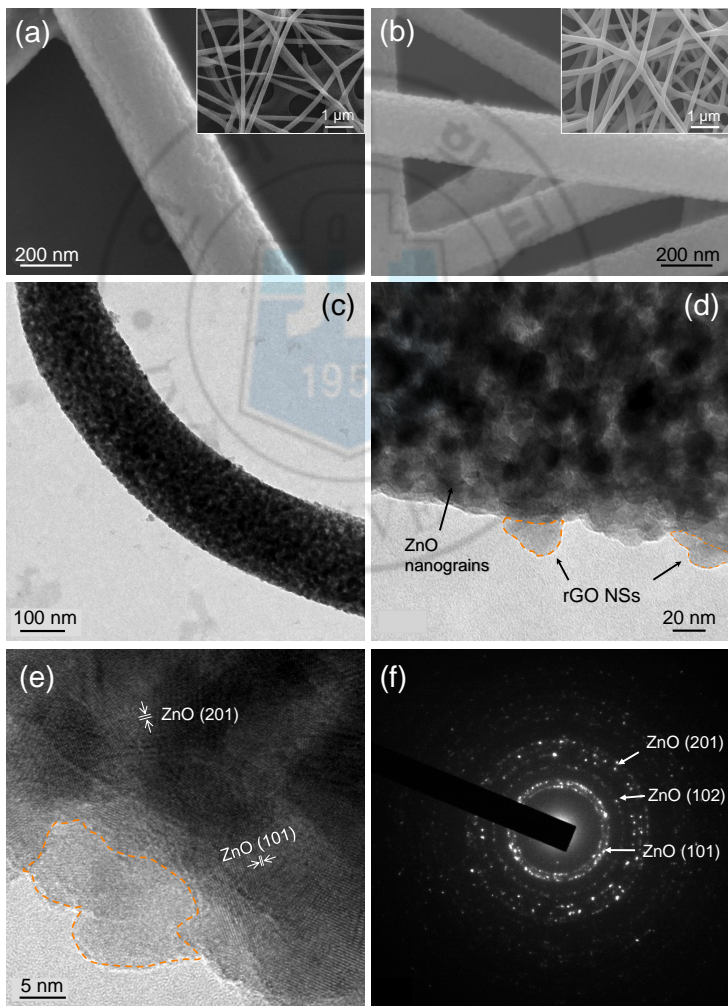
FIGURE 4.1: Microstructural analysis of RGO-loaded ZnO nanofibers
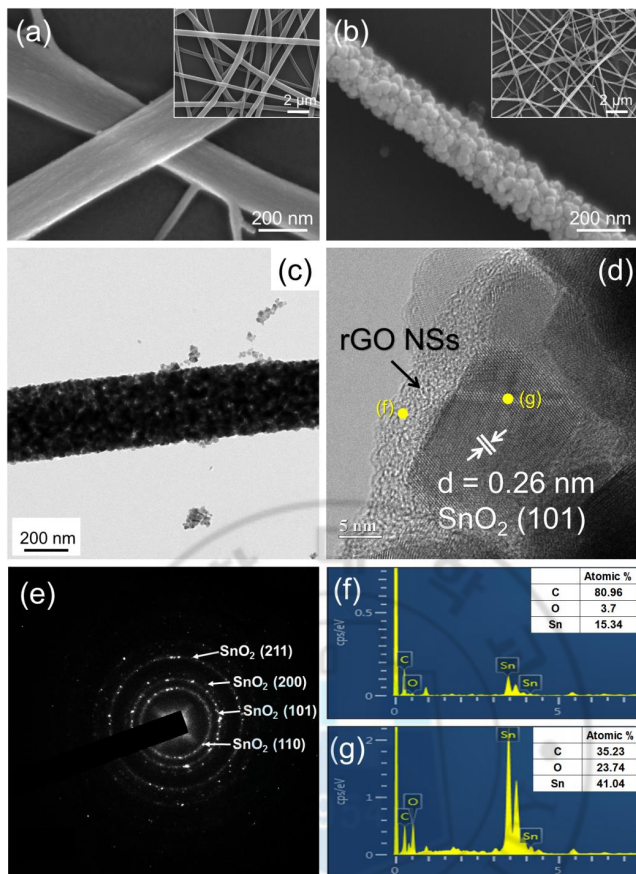
FIGURE 4.2: Microstructural analysis of RGO-loaded SnO_2 nanofibers

and 450 °C. The sensing behavior of both sensors was similar to a typical *n*-type
oxide semiconductor (*i.e*, a decrease in resistance by a reducing gas; (Figure 4.3).
The sensor responses of both sensors monotonically increased with increasing not
only hydrogen gas concentration but also temperature.

It is noteworthy that RGO-loaded ZnO nanofibers exhibited the highest
responses than RGO-loaded SnO_2 nanofibers at all temperatures even to a trace
amount of hydrogen (100 ppb), demonstrating its potential use in selective
detection of hydrogen in a harsh environment. The sensor responses of
RGO-loaded SnO_2 nanofibers and RGO-loaded ZnO nanofibers are 74.8 and 2524,
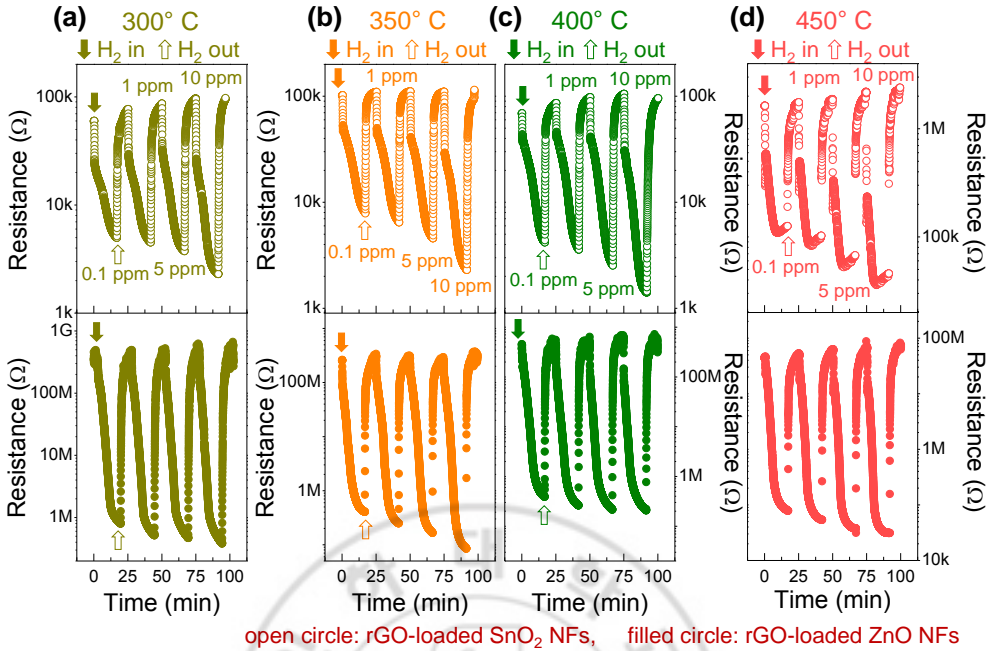
FIGURE 4.3: Resistance curves of RGO-loaded SnO_2 and RGO-loaded ZnO composite nanofibers at various temperatures

TABLE 4.1: Responses of RGO loaded SnO_2 and RGO loaded ZnO composite nanofibers

H_2 concentration	Responses (R_a/R_g)							
	RGO loaded SnO_2 composite				RGO loaded ZnO composite			
	300 °C	350 °C	400 °C	450 °C	300 °C	350 °C	400 °C	450 °C
100 ppb	12.1	13.0	16.5	12.9	422.9	485.3	865.9	581.0
1 ppm	17.1	17.0	24.0	17.2	721.3	1019.3	1415.4	957.9
5 ppm	23.2	24.2	38.7	27.2	852.6	1593.2	2010.3	1657.4
10 ppm	42.0	47.8	74.8	41.8	1007.5	1731.6	2524.0	2028.0

respectively, to 10 ppm of hydrogen gas at 400 °C (Table 4.1).

Also, the RGO-loaded ZnO nanofibers were found to be extremely selectively sensitive to H_2 gas, in comparison to other gases, including NO_2, SO_2, O_2, CO, C_6H_6, and C_2H_5OH (Table 4.2).

Figure 4.5 shows the change of sensor responses of RGO-loaded SnO_2 nanofibers and RGO-loaded ZnO nanofibers with varying the sensing temperature

TABLE 4.2: Responses of 0.44 wt% RGO loaded ZnO nanofibers to various gases at 400
°C

Gases	Responses (R_a/R_g or R_g/R_a)		
	1 ppm	2 ppm	5 ppm
NO_2	91.5	110.0	119.0
SO_2	49.7	59.5	65.7
O_2	23.2	28.8	34.2
CO	7.7	9.7	22.6
C_6H_6	14.4	15.7	19.1
C_2H_5OH	14.9	15.8	19.1
H_2	1415.4	2010.3	2524.0

in the range of 300-450 °C at H_2 concentration of 10 ppm. The sensor responses of
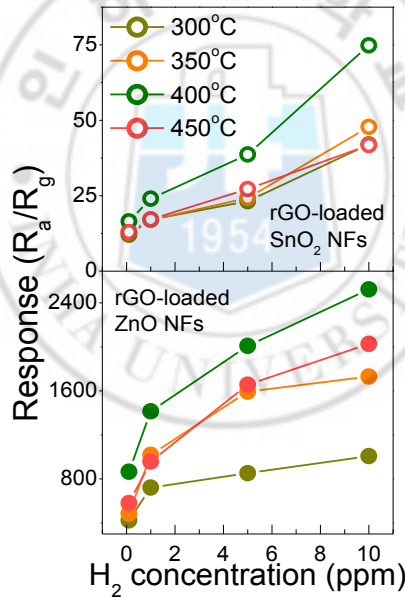
FIGURE 4.4: Responses of RGO-loaded SnO_2 and RGO-loaded ZnO composite nanofibers
at various temperatures as a function of H_2 concentration

RGO-loaded ZnO nanofibers are 1007.5, 1731.6, and 2524.0 and 2028.0, at 300,

350, 400 and 450 °C, respectively, whereas those of RGO-loaded SnO_2 nanofibers

were 42.0, 47.8, 74.8, and 41.8, indicating that RGO-loaded ZnO nanofibers have

significantly higher sensitivities than RGO-loaded SnO_2 nanofibers.

In addition, the additional increase in the sensor response of RGO-loaded ZnO nanofibers with increasing temperature will be associated with an enhancement of ZnO metallization at a higher temperature. Alternatively, it is expected that the metallization of ZnO will be dependent on the sensing temperature, with hydrogen atoms inducing metallization of ZnO even at room temperature. First, the diffusion coefficient of interstitial hydrogen D_H in ZnO is known to increase drastically by increasing the temperature from room temperature to 800 K. Accordingly, the amount of H-loading on the ZnO surface will increase
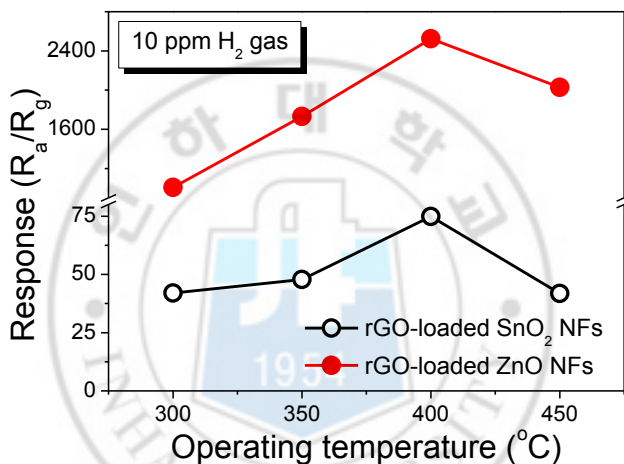
FIGURE 4.5: Response of RGO-loaded ZnO and RGO-loaded SnO_2 nanofibers for 10 ppm H_2

by increasing the sensing temperature. Second, the associated metallization reactions are thermodynamically favorable at higher temperatures.

$$ZnO_{(s)} + H_{2(g)} \longrightarrow Zn_{(s)} + H_2O_{(g)}$$
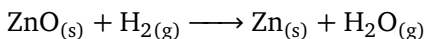
With adopting the standard free energy as $\Delta G° = 130,415-119.353T$ (kJ/mol), those at 300, 350, and 400 °C are calculated to be about 62.01, 56.04, and 50.07 kJ/mol, respectively.

In addition, it is possible that hydrogen adsorbed on Zn-polar surface is so reactive that it is able to reducing ZnO to metallic Zn, forming and desorbing OH

groups by the following equation:

$$ZnO_{(s)} + H_{(g)} \longrightarrow Zn_{(s)} + OH_{(g)}$$
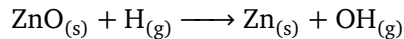
With adopting the standard free energy as $\Delta G° = 171{,}448\text{-}66.984T$ (kJ/mol), those at 300, 350, and 400 °C are calculated to be about 133.06, 129.71, and 126.36 kJ/mol, respectively. Although the present sensing is not in its standard condition, the Zn metallization will be thermodynamically favorable at higher temperature.

The sensor response curves exhibited a bell-shaped behavior, with the maximum value at 400 °C. The possible reasons for the bell-shaped behavior are explained as follows:

It has been revealed that the maximum sensing temperature of metal oxides such as SnO_2 and ZnO can be varied over large temperature range, depending on many factors, which are not yet clearly known. There are several factors which affect the hydrogen sensing behavior. First, the redox reaction, in which the hydrogen molecules will react with the adsorbed oxygen species, is exothermic and will be activated or enhanced at higher temperature. Second, the adsorption and desorption of hydrogen will be important. At higher temperature, the adsorption of hydrogen will be suppressed and may be desorbed prior to the redox reaction, contributing to the depression of hydrogen sensing at higher temperature. Third, in case of ZnO sensor, hydrogen-induced metallization will affect the sensing behavior. The Zn metallization will be thermodynamically favorable at higher temperature. Accordingly, with the adsorption being suppressed at higher temperature, it is expected that the temperature-dependent sensing exhibits the bell-shaped behavior.

We have compared the sensor responses of RGO-loaded ZnO nanofibers to those of RGO-loaded SnO_2 nanofibers, pure SnO_2 nanofibers, and pure ZnO nanofibers, with respect to H_2 gas. The H_2 concentration was fixed to 10 ppm

as shown in Figure 4.6. Not only the use of ZnO but also the introduction of RGO
played crucial roles in enhancing the sensing behavior.
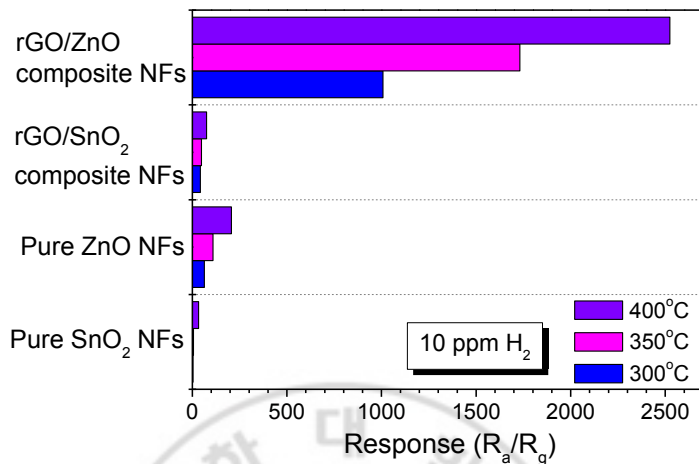
FIGURE 4.6: Responses of pure SnO_2, pure ZnO, RGO-loaded SnO_2 and RGO-loaded ZnO
nanofibers at various temperatures

4.3.3   Sensing Mechanism

The main sensing mechanisms in ZnO nanofibers are explained here. First, there
is resistance modulation due to the change in the radial thickness of the electron
depletion layer, underneath the surface. The depletion layer will be contracted
and expanded, by the introduction and removal of H_2 gas, respectively. Second,
excellent gas sensing characteristics of nanofibers were ascribed to the presence
of grain boundaries, establishing the potential barriers and thus upward band
bending at the grain boundaries in ambient air.

Upon introduction of H_2 gas, H_2 molecules adsorb and react with chemisorbed
oxygen in the ZnO grain boundaries, reducing the potential barriers and thus
increasing the conductivity.   While the resistance modulation through the
introduction/removal of a target gas is a generally accepted mechanism for
metal oxide nanofibers-based gas sensors, the exceptionally high responses of the

p-rGO – metallic Zn in H$_2$ gas

$\Phi_{ZnO} > \Phi_{rGO} > \Phi_{Zn}$

In air (Oxygen adsorbed)

Hydrogen Environment

In H$_2$ (H$_2$ adsorbed) Metallic Zn surface

Modulation of potential barriers by surface metallization of ZnO nanograins

E_c
E_f

p-rGO   n-ZnO

E_c
E_f

rGO   Zn$_{metallic}$ ZnO

p-rGO NSs   n-ZnO nanograins   Depleted layer   Zn$_{metallic}$
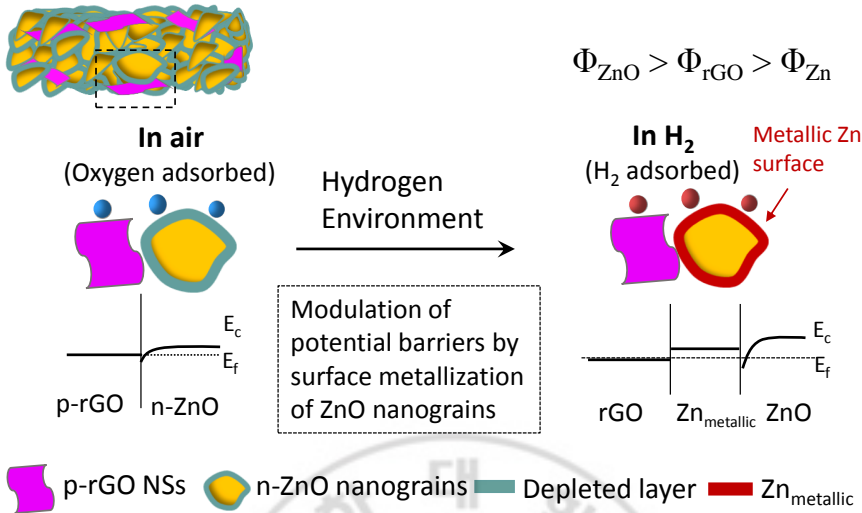
FIGURE 4.7: Sensing mechanisms in which the surface of the ZnO nanograin is metallized

present nanofibers to H$_2$ gas indicate additional resistance modulation. Several studies have reported the creation of heterointerfaces between a metal oxide and graphene [78, 143, 144] for improving the sensing properties. Similarly, compared to pure SnO$_2$ nanofibers, the sensing responses of RGO-loaded SnO$_2$ nanofibers were significantly enhanced due to the presence of RGO [78].

Additionally, the superior response of RGO-loaded ZnO nanofibers with respect to that of RGO-loaded SnO$_2$, in conjunction with the observation that pure ZnO nanofibers exhibit a superior sensor response to pure SnO$_2$ nanofibers, suggests that the interaction of H$_2$ with RGO-loaded ZnO noticeably affects the sensing behavior. Since the introduction of H$_2$ gas inevitably generates a metallic Zn layer along the RGO/ZnO heterojunctions, the energy band diagrams involving three phases should be considered (Figure 4.7). From the differences in work functions, at equilibrium, the potential barriers will be generated not only at the RGO/Zn interfaces but also at the Zn/ZnO interfaces.

First, the *n*-ZnO will become more *n*-type, by the transfer of electrons from

metallic Zn. With the enlarged ZnO depletion region on the nanofibers surface, the introduction/removal of H_2 will generate the relatively larger resistance modulation. Second, in ambient H_2, the potential barrier of RGO/Zn prevents the electron flow into RGO. Accordingly, the electrons in the ZnO region of sensor devices will not be lost to the RGO region. This will further decrease the resistance, which will be induced by the introduction of H_2 gas. Third, the RGO nanosheets will exert the spillover effect, enhancing the sensing behavior. Based on our results, the extraordinary improvement in the sensing properties of RGO-loaded ZnO nanofibers for H_2 is primarily due to the surface metallization effect (occurring in a H_2 atmosphere) combined with the creation of local *p-n* heterojunctions.

Although extraordinarily high sensor responses were observed from sensors consisting of SnO_2 thin films [145, 146], the H_2 concentration was in the range of 800-1000 ppm. Despite the importance of hydrogen sensor operation at low concentrations, there have been few studies on such sensors. The Bi_2S_3 nanowire-based sensors exhibited a room-temperature sensor response of 1.22 at 10 ppm [147]. B. Wang *et al*. reported a sensor response <0.5 at 10 ppm using SnO_2 nanowires [148]. We recently developed a ZnO nanofibers based sensor, showing a H_2 detection response of 63.8 at a very low concentration of 0.1 ppm. This striking enhancement in H_2 sensitivity was ascribed to the hydrogen-induced metallization on the surface of ZnO nanograins [137].

This work presents the highest response to date to a very small concentration of H_2 with short recovery times. Experimental results suggest that RGO-loaded ZnO-based gas sensors can be applied when very low H_2 detection is required due to the combined effect of *p*-RGO and the semiconductor-to-metal transition effect of ZnO in a H_2 atmosphere. However, better responses with more rapid responses and recovery times at a relatively low temperature can be obtained by tuning the heterointerfaces between *p*-RGO nanosheets and *n*-ZnO nanograins and

through functionalization or electronic sensitization with palladium or platinum nanoparticles. This study is in progress and will be presented in the following reports.

4.4 Summary

In summary, uniformly-distributed RGO-loaded metal oxide composite nanofibers with average diameters of 190 nm were synthesized through a low-cost electrospinning process. These RGO-loaded nanofibers had a polycrystalline nature due to the presence of a large number of nanograins, which were responsible for the additional resistance modulation at grain boundaries. The p-RGO nanosheets attached to the nanofibers greatly enhanced the sensing properties of the nanofibers by creating local heterointerfaces with the n-type nanograins and acted as electron acceptors. At 10 ppm of H_2, the RGO-loaded ZnO nanofibers exhibited a sensor response of approximately 2524. The RGO-loaded ZnO nanofibers exhibited excellent sensor responses (865.9) to a very low concentration of H_2 gas (100 ppb).

These enhanced and extraordinary improvements in the sensing properties of RGO-loaded ZnO nanofibers were attributed to the combined effect of (i) the presence of p-RGO nanosheets and (ii) semiconductor-to-metal transition of ZnO in a H_2 atmosphere. The present study provides a powerful insight into the enhancement of sensing abilities and selectivities due to the incorporation of RGO nanosheets and ZnO-based gas sensors for detecting trace amounts of H_2.

Chapter 5

Concluding Remarks

This chapter is devoted to conclusions and main findings of this research work and future recommendations for this investigation.

5.1   Conclusions

This research work can be concluded as follows

- Graphene and reduced graphene loaded composite metal oxide (SnO_2 and ZnO, respectively) nanofibers were synthesized using a low cost and facile electrospinning process and various low concentrations of oxidizing and reducing gases were tested at a variety of operating temperatures.

- The amounts of graphene and reduced graphene oxide as well as the operating temperature were optimized for best sensing performances.

- Microstructural and morphological analysis were carried out using XRD, FE-SEM, HR-TEM *etc.* and these analysis confirmed the presence of graphene and reduced graphene oxide nanosheets in the polycrystalline metal oxide nanofibers. These analyses were helpful to understand

the interaction of p-type graphene or reduced graphene oxide with the nanograins of n-type metal oxides.

- The sensitivity of the graphene or reduced graphene oxide loaded composite nanofibers were significantly enhanced as compared to the pristine metal oxide nanofibers.

- Reduced graphene oxide loaded ZnO nanofibers showed exceptionally high sensitivity and selectivity towards the low concentration of hydrogen gas.

Various novel hybrid sensing mechanisms have been proposed for better sensitivities and selectivity of the fabricated gas sensors.

5.2   Outlook

Although, this research has explored and established the sensing behavior of graphene loaded metal oxide nanocomposites, further research could be undertaken to improve the sensing performances and for better understanding of sensing mechanisms of the fabricated sensors by

- expanding the range (lower and higher) of gas concentration and operating temperature of the sensor to improve their sensitivity and selectivity

- increasing the target gas variety (*e.g,* more hydrocarbons, alcohols and other reducing and toxic gases *etc.*) to ascertain the selectivity of the sensors

- studying the effects of deposition duration on the behavior of gas sensitivity

- the stability of the obtained sensors should be confirmed by long term tests under real working conditions such as in humid environments

The author believes that this work could also be extended to investigate the gas sensing mechanisms at the nanoscale using density functional theory (DFT)

modeling and finite element modeling (FEM) and simulations. This atomistic simulation will provide details of the transport properties of the carriers in the composite nanostructures so that the sensing device can be accurately designed for the maximum performance.

Finally, an integrated micro machined gas sensor array, associated with pattern recognition (PARC) techniques, such as artificial neural networks (ANNs), could be studied and analyzed to overcome the problems associated with poor selectivity encountered during the operation of individual gas sensor.

Bibliography

[1] M. J. Madou and S. R. Morrison, *Chemical sensing with solid state devices*, Academic Press, San Diego, 1989, DOI: 10.1016/B978-0-12-464965-1.50006-5.

[2] C. G. B. Garrett and W. H. Brattain, *Physical Review*, 1955, **99**, 376–387, DOI: 10.1103/PhysRev.99.376.

[3] W. H. Brattain and C. G. B. Garrett, *Physica*, 1954, **20**, 885–892, DOI: 10.1016/s0031-8914(54)80200-x.

[4] A. BielaNSki, J. DereN and J. Haber, *Nature*, 1957, **179**, 668–669, DOI: 10.1038/179668a0.

[5] T. Seiyama, A. Kato, K. Fujiishi and M. Nagatani, *Analytical Chemistry*, 1962, **34**, 1502–1503, DOI: 10.1021/ac60191a001.

[6] T. Naoyoshi, *Gas-detecting device*, 1971, US Patent 3,631,436.

[7] N. Yamazoe, G. Sakai and K. Shimanoe, *Catalysis Surveys from Asia*, 2003, **7**, 63–75, DOI: 10.1023/A:1023436725457.

[8] N. Yamazoe, *Sensors and Actuators B: Chemical*, 1991, **5**, 7–19, DOI: 10.1016/0925-4005(91)80213-4.

[9] S. R. Morrison, *Sensors and Actuators*, 1987, **12**, 425–440, DOI: 10.1016/0250-6874(87)80061-6.

[10] N. Yamazoe, Y. Kurokawa and T. Seiyama, *Sensors and Actuators B: Chemical*, 1983, **4**, 283–289, DOI: 10.1016/0250-6874(83)85034-3.

[11] N. Yamazoe, *Sensors and Actuators B: Chemical*, 2005, **108**, 2–14, DOI: 10.1016/j.snb.2004.12.075.

[12] D. R. Miller, S. A. Akbar and P. A. Morris, *Sensors and Actuators B: Chemical*, 2014, **204**, 250–272, DOI: 10.1016/j.snb.2014.07.074.

[13] E. Comini, M. Ferroni, V. Guidi, G. Faglia, G. Martinelli and G. Sberveglieri, *Sensors and Actuators B: Chemical*, 2002, **84**, 26–32, DOI: 10.1016/S0925-4005(02)00006-0.

[14] V. Dobrokhotov, D. N. McIlroy, M. G. Norton, A. Abuzir, W. J. Yeh, I. Stevenson, R. Pouy, J. Bochenek, M. Cartwright, L. Wang, J. Dawson, M. Beaux and C. Berven, *Journal of Applied Physics*, 2006, **99**, 104302–104309, DOI: 10.1063/1.2195420.

[15] W. C. Conner and J. L. Falconer, *Chemical Reviews*, 1995, **95**, 759–788, DOI: 10.1021/Cr00035a014.

[16] U. Heiz and E. L. Bullock, *Journal of Materials Chemistry*, 2004, **14**, 564–577, DOI: 10.1039/b313560h.

[17] D. Barreca, E. Comini, A. P. Ferrucci, A. Gasparotto, C. Maccato, C. Maragno, G. Sberveglieri and E. Tondello, *Chemistry of Materials*, 2007, **19**, 5642–5649, DOI: 10.1021/cm701990f.

[18] J. Zhang, X. Liu, L. Wang, T. Yang, X. Guo, S. Wu, S. Wang and S. Zhang, *Nanotechnology*, 2011, **22**, 185501–185508, DOI: 10.1088/0957-4484/22/18/185501.

[19] M. E. Franke, T. J. Koplin and U. Simon, *Small*, 2006, **2**, 36–50, DOI: 10.1002/smll.200500261.

[20] Z. L. Wang, *Advanced Materials*, 2000, **12**, 1295–1298, DOI: 10.1002/1521-4095(200009)12:17<1295::AID-ADMA1295>3.0.CO;2-B.

[21] J. D. Prades, R. Jimenez-Diaz, F. Hernandez-Ramirez, S. Barth, A. Cirera, A. Romano-Rodriguez, S. Mathur and J. R. Morante, *Applied Physics Letters*, 2008, **93**, 123110–123113, DOI: 10.1063/1.2988265.

[22] E. Comini, C. Baratto, I. Concina, G. Faglia, M. Falasconi, M. Ferroni, V. Galstyan, E. Gobbi, A. Ponzoni, A. Vomiero, D. Zappa, V. Sberveglieri and G. Sberveglieri, *Sensors and Actuators B: Chemical*, 2013, **179**, 3–20, DOI: 10.1016/j.snb.2012.10.027.

[23] E. Comini, C. Baratto, G. Faglia, M. Ferroni, A. Vomiero and G. Sberveglieri, *Progress in Materials Science*, 2009, **54**, 1–67, DOI: 10.1016/j.pmatsci.2008.06.003.

[24] D. H. Reneker and A. L. Yarin, *Polymer*, 2008, **49**, 2387–2425, DOI: 10.1016/j.polymer.2008.02.002.

[25] J. Doshi and D. H. Reneker, *Journal of Electrostatics*, 1995, **35**, 151–160, DOI: 10.1016/0304-3886(95)00041-8.

[26] J. P. Lagerwall, J. T. McCann, E. Formo, G. Scalia and Y. Xia, *Chemical Communications*, 2008, 5420–5422, DOI: 10.1039/b810450f.

[27] P. D. Dalton, D. Grafahrend, K. Klinkhammer, D. Klee and M. Moller, *Polymer*, 2007, **48**, 6823–6833, DOI: 10.1016/j.polymer.2007.09.037.

[28] A. V. Bazilevsky, A. L. Yarin and C. M. Megaridis, *Langmuir*, 2007, **23**, 2311–2314, DOI: 10.1021/la063194q.

[29] A. L. Yarin, E. Zussman, J. H. Wendorff and A. Greiner, *Journal of Materials Chemistry*, 2007, **17**, 2585–2599, DOI: 10.1039/b618508h.

[30] C. J. Luo, S. D. Stoyanov, E. Stride, E. Pelan and M. Edirisinghe, *Chemical Society Reviews*, 2012, **41**, 4708–4735, DOI: 10.1039/c2cs35083a.

[31] R. Ramaseshan, S. Sundarrajan, R. Jose and S. Ramakrishna, *Journal of Applied Physics*, 2007, **102**, 111101–111118, DOI: 10.1063/1.2815499.

[32] D. Li, J. T. McCann and Y. N. Xia, *Journal of the American Ceramic Society*, 2006, **89**, 1861–1869, DOI: 10.1111/j.1551-2916.2006.00989.x.

[33] D. Li and Y. Xia, *Advanced Materials*, 2004, **16**, 1151–1170, DOI: 10.1002/adma.200400719.

[34] R. Kessick, J. Fenn and G. Tepper, *Polymer*, 2004, **45**, 2981–2984, DOI: 10.1016/j.polymer.2004.02.056.

[35] A. L. Yarin, S. Koombhongse and D. H. Reneker, *Journal of Applied Physics*, 2001, **90**, 4836–4846, DOI: 10.1063/1.1408260.

[36] M. M. Hohman, M. Shin, G. Rutledge and M. P. Brenner, *Physics of Fluids*, 2001, **13**, 2201–2220, DOI: 10.1063/1.1383791.

[37] S. V. Fridrikh, J. H. Yu, M. P. Brenner and G. C. Rutledge, *Physical Review Letters*, 2003, **90**, 144502–144506, DOI: 10.1103/PhysRevLett.90.144502.

[38] X. Lu, C. Wang and Y. Wei, *Small*, 2009, **5**, 2349–2370, DOI: 10.1002/smll.200900445.

[39] A. Katoch, S. W. Choi and S. S. Kim, *Metals and Materials International*, 2015, **21**, 213–221, DOI: 10.1007/s12540-015-4319-8.

[40] A. Katoch, J. H. Kim and S. S. Kim, *Journal of Sensors*, 2015, **2015**, 1–7, DOI: 10.1155/2015/387641.

[41] A. Katoch, S. W. Choi, G. J. Sun, H. W. Kim and S. S. Kim, *Nanotechnology*, 2014, **25**, 175501–175508, DOI: 10.1088/0957-4484/25/17/175501.

[42] J. Y. Park, S. W. Choi, J. W. Lee, C. Lee and S. S. Kim, *Journal of the American Ceramic Society*, 2009, **92**, 2551–2554, DOI: 10.1111/j.1551-2916.2009.03270.x.

[43] A. Katoch, J. H. Kim and S. S. Kim, *ACS Applied Materials & Interfaces*, 2014, **6**, 21494–21499, DOI: 10.1021/am506499e.

[44] Z. J. Wang, Z. Y. Li, J. H. Sun, H. N. Zhang, W. Wang, W. Zheng and C. Wang, *Journal of Physical Chemistry C*, 2010, **114**, 6100–6105, DOI: 10.1021/jp9100202.

[45] X. J. Zhang and G. J. Qiao, *Applied Surface Science*, 2012, **258**, 6643–6647, DOI: 10.1016/j.apsusc.2012.03.098.

[46] C.-S. Lee, I.-D. Kim and J.-H. Lee, *Sensors and Actuators B: Chemical*, 2013, **181**, 463–470, DOI: 10.1016/j.snb.2013.02.008.

[47] C. Feng, X. Li, J. Ma, Y. Sun, C. Wang, P. Sun, J. Zheng and G. Lu, *Sensors and Actuators B: Chemical*, 2015, **209**, 622–629, DOI: 10.1016/j.snb.2014.12.019.

[48] C. Feng, C. Wang, P. Cheng, X. Li, B. Wang, Y. Guan, J. Ma, H. Zhang, Y. Sun, P. Sun, J. Zheng and G. Lu, *Sensors and Actuators B: Chemical*, 2015, **221**, 434–442, DOI: 10.1016/j.snb.2015.06.114.

[49] W. F. Qin, L. Xu, J. Song, R. Q. Xing and H. W. Song, *Sensors and Actuators B: Chemical*, 2013, **185**, 231–237, DOI: 10.1016/j.snb.2013.05.001.

[50] H. Y. Du, J. Wang, M. Y. Su, P. J. Yao, Y. G. Zheng and N. S. Yu, *Sensors and Actuators B: Chemical*, 2012, **166**, 746–752, DOI: 10.1016/j.snb.2012.03.055.

[51] C. Feng, W. Li, C. Li, L. Zhu, H. Zhang, Y. Zhang, S. Ruan, W. Chen and L. Yu, *Sensors and Actuators B: Chemical*, 2012, **166-167**, 83–88, DOI: 10.1016/j.snb.2011.12.083.

[52] A. A. Aksenov, M. Schivo, H. Bardaweel, Y. Zrodnikov, A. M. Kwan, K. Zamuruyev, W. H. K. Cheung, D. J. Peirano and C. E. Davis, in *Volatile organic compounds in human breath: Biogenic origin and point-of-care analysis approaches*, ed. A. Amann and D. Smith, Elsevier, UK, 1st edn., 2013, pp. 129–154, DOI: 10.1016/b978-0-44-462613-4.00008-8.

[53] W. Miekisch, J. K. Schubert and G. F. Noeldge-Schomburg, *Clinica Chimica Acta*, 2004, **347**, 25–39, DOI: 10.1016/j.cccn.2004.04.023.

[54] I. Ahmed, R. Greenwood, L. Costello Bde, N. M. Ratcliffe and C. S. Probert, *PLOS One*, 2013, **8**, e58204–e58217, DOI: 10.1371/journal.pone.0058204.

[55] M. Gallagher, C. J. Wysocki, J. J. Leyden, A. I. Spielman, X. Sun and G. Preti, *British Journal of Dermatology*, 2008, **159**, 780–791, DOI: 10.1111/j.1365-2133.2008.08748.x.

[56] L. Pauling, A. B. Robinson, R. Teranishi and P. Cary, *Proceedings of the National Academy of Sciences of the United States of America*, 1971, **68**, 2374–2376, DOI: 10.1073/pnas.68.10.2374.

[57] K. Schmidt and I. Podmore, *Journal of Biomarkers*, 2015, **2015**, 981458, DOI: 10.1155/2015/981458.

[58] Y. Y. Broza and H. Haick, *Nanomedicine*, 2013, **8**, 785–806, DOI: 10.2217/nnm.13.64.

[59] G. Konvalina and H. Haick, *Accounts of Chemical Research*, 2014, **47**, 66–76, DOI: 10.1021/ar400070m.

[60] M. Hakim, Y. Y. Broza, O. Barash, N. Peled, M. Phillips, A. Amann and H. Haick, *Chemical Reviews*, 2012, **112**, 5949–5966, DOI: 10.1021/cr300174a.

[61] K. H. Kim, S. A. Jahan and E. Kabir, *TrAC Trends in Analytical Chemistry*, 2012, **33**, 1–8, DOI: 10.1016/j.trac.2011.09.013.

[62] J. Pereira, P. Porto-Figueira, C. Cavaco, K. Taunk, S. Rapole, R. Dhakne, H. Nagarajaram and J. S. Camara, *Metabolites*, 2015, **5**, 3–55, DOI: 10.3390/metabo5010003.

[63] M. Righettoni, A. Amann and S. E. Pratsinis, *Materials Today*, 2015, **18**, 163–171, DOI: 10.1016/j.mattod.2014.08.017.

[64] J. Zhang, X. Liu, G. Neri and N. Pinna, *Advanced Materials*, 2016, **28**, 795–831, DOI: 10.1002/adma.201503825.

[65] Y. Zhao, X. L. He, J. P. Li, X. G. Gao and J. Jia, *Sensors and Actuators B: Chemical*, 2012, **165**, 82–87, DOI: 10.1016/j.snb.2012.02.020.

[66] J. Kong, N. R. Franklin, C. W. Zhou, M. G. Chapline, S. Peng, K. J. Cho and H. J. Dai, *Science*, 2000, **287**, 622–625, DOI: 10.1126/science.287.5453.622.

[67] Z. U. Abideen, H. W. Kim and S. S. Kim, *Chemical Communications*, 2015, **51**, 15418–15421, DOI: 10.1039/c5cc05370f.

[68] Z. U. Abideen, A. Katoch, J. H. Kim, Y. J. Kwon, H. W. Kim and S. S. Kim, *Sensors and Actuators B: Chemical*, 2015, **221**, 1499–1507, DOI: 10.1016/j.snb.2015.07.120.

[69] S. Gadipelli and Z. X. Guo, *Progress in Materials Science*, 2015, **69**, 1–60, DOI: 10.1016/j.pmatsci.2014.10.004.

[70] J. van den Brink, *Nature Nanotechnology*, 2007, **2**, 199–201, DOI: 10.1038/nnano.2007.91.

[71] F. Schedin, A. K. Geim, S. V. Morozov, E. W. Hill, P. Blake, M. I. Katsnelson and K. S. Novoselov, *Nature Materials*, 2007, **6**, 652–655, DOI: 10.1038/nmat1967.

[72] S. Gupta Chatterjee, S. Chatterjee, A. K. Ray and A. K. Chakraborty, *Sensors and Actuators B: Chemical*, 2015, **221**, 1170–1181, DOI: 10.1016/j.snb.2015.07.070.

[73] S. S. Varghese, S. Lonkar, K. K. Singh, S. Swaminathan and A. Abdala, *Sensors and Actuators B: Chemical*, 2015, **218**, 160–183, DOI: 10.1016/j.snb.2015.04.062.

[74] G. S. Kulkarni, K. Reddy, Z. Zhong and X. Fan, *Nature Communications*, 2014, **5**, 4376–4383, DOI: 10.1038/ncomms5376.

[75] T. Van Khai, H. G. Na, D. S. Kwak, Y. J. Kwon, H. Ham, K. B. Shim and H. W. Kim, *Journal of Materials Chemistry*, 2012, **22**, 17992, DOI: 10.1039/c2jm33194b.

[76] W. S. Hummers and R. E. Offeman, *Journal of the American Chemical Society*, 1958, **80**, 1339–1339, DOI: 10.1021/ja01539a017.

[77] S. W. Choi, J. Y. Park and S. S. Kim, *Nanotechnology*, 2009, **20**, 465603–465603, DOI: 10.1088/0957-4484/20/46/465603.

[78] J. H. Lee, A. Katoch, S. W. Choi, J. H. Kim, H. W. Kim and S. S. Kim, *ACS Applied Materials & Interfaces*, 2015, **7**, 3101–3109, DOI: 10.1021/am5071656.

[79] J. Y. Park, S. W. Choi and S. S. Kim, *Nanoscale Research Letters*, 2009, **5**, 353–359, DOI: 10.1007/s11671-009-9487-3.

[80] S. J. Choi, B. H. Jang, S. J. Lee, B. K. Min, A. Rothschild and I. D. Kim, *ACS Applied Materials & Interfaces*, 2014, **6**, 2588–2597, DOI: 10.1021/am405088q.

[81] N. Tammanoon, A. Wisitsoraat, C. Sriprachuabwong, D. Phokharatkul, A. Tuantranont, S. Phanichphant and C. Liewhiran, *ACS Applied Materials & Interfaces*, 2015, **7**, 24338–24352, DOI: 10.1021/acsami.5b09067.

[82] J. H. Kim, A. Katoch, H. W. Kim and S. S. Kim, *Chemical Communications*, 2016, **52**, 3832–3835, DOI: 10.1039/c5cc10482c.

[83] V. V. Malyshev and A. V. Pislyakov, *Sensors and Actuators B: Chemical*, 2008, **134**, 913–921, DOI: 10.1016/j.snb.2008.06.046.

[84] M. Cao, Y. Wang, T. Chen, M. Antonietti and M. Niederberger, *Chemistry of Materials*, 2008, **20**, 5781–5786, DOI: 10.1021/cm800794y.

[85] A. Tangerman and E. G. Winkel, *Journal of Breath Research*, 2010, **4**, 017003–017009, DOI: 10.1088/1752-7155/4/1/017003.

[86] V. I. Hegde, S. N. Shirodkar, N. Tit, U. V. Waghmare and Z. H. Yamani, *Surface Science*, 2014, **621**, 168–174, DOI: 10.1016/j.susc.2013.11.015.

[87] E. Mohammadi-Manesh, M. Vaezzadeh and M. Saeidi, *Surface Science*, 2015, **636**, 36–41, DOI: 10.1016/j.susc.2015.02.002.

[88] M. Asad, M. H. Sheikhi, M. Pourfath and M. Moradid, *Sensors and Actuators B: Chemical*, 2015, **210**, 1–8, DOI: 10.1016/j.snb.2014.12.086.

[89] D. Zhang, F. Xie, P. Lin and W. C. Choy, *ACS Nano*, 2013, **7**, 1740–1747, DOI: 10.1021/nn3058399.

[90] S. S. Li, K. H. Tu, C. C. Lin, C. W. Chen and M. Chhowalla, *ACS Nano*, 2010, **4**, 3169–3174, DOI: 10.1021/nn100551j.

[91] S. M. Song, J. K. Park, O. J. Sul and B. J. Cho, *Nano Letters*, 2012, **12**, 3887–3892, DOI: 10.1021/nl300266p.

[92] K. R. Ratinac, W. Yang, S. P. Ringer and F. Braet, *Environmental Science & Technology*, 2010, **44**, 1167–1176, DOI: 10.1021/es902659d.

[93] J. Ding, J. W. Zhu, P. C. Yao, J. Li, H. P. Bi and X. Wang, *Industrial & Engineering Chemistry Research*, 2015, **54**, 8947–8953, DOI: 10.1021/acs.iecr.5b01711.

[94] H. Y. Huang, P. C. Xu, D. Zheng, C. Z. Chen and X. X. Li, *Journal of Materials Chemistry A*, 2015, **3**, 6330–6339, DOI: 10.1039/c4ta05963h.

[95] A. Tricoli, M. Righettoni and A. Teleki, *Angewandte Chemie International Edition*, 2010, **49**, 7632–59, DOI: 10.1002/anie.200903801.

[96] M. M. Arafat, B. Dinan, S. A. Akbar and A. S. Haseeb, *Sensors*, 2012, **12**, 7207–58, DOI: 10.3390/s120607207.

[97] Z. Li, H. Zhang, W. Zheng, W. Wang, H. Huang, C. Wang, A. G. MacDiarmid and Y. Wei, *Journal of the American Chemical Society*, 2008, **130**, 5036–7, DOI: 10.1021/ja800176s.

[98] Z. M. Huang, Y. Z. Zhang, M. Kotaki and S. Ramakrishna, *Composites Science and Technology*, 2003, **63**, 2223–2253, DOI: 10.1016/S0266-3538(03)00178-7.

[99] Y. Zhang, X. L. He, J. P. Li, Z. J. Miao and F. Huang, *Sensors and Actuators B: Chemical*, 2008, **132**, 67–73, DOI: 10.1016/j.snb.2008.01.006.

[100] Z. Zhang, X. Li, C. Wang, L. Wei, Y. Liu and C. Shao, *Journal of Physical Chemistry C*, 2009, **113**, 19397–19403, DOI: 10.1021/jp9070373.

[101] G. Wang, Y. Ji, X. Huang, X. Yang, P. I. Gouma and M. Dudley, *Journal of Physical Chemistry B*, 2006, **110**, 23777–23782, DOI: 10.1021/jp0635819.

[102] D. J. Yang, I. Kamienchick, D. Y. Youn, A. Rothschild and I. D. Kim, *Advanced Functional Materials*, 2010, **20**, 4258–4264, DOI: 10.1002/adfm.201001251.

[103] W. E. Teo and S. Ramakrishna, *Nanotechnology*, 2006, **17**, R89–R106, DOI: 10.1088/0957-4484/17/14/R01.

[104] C. Lee, S. W. Choi, J. Y. Park and S. S. Kim, *Sensor Letters*, 2011, **9**, 132–136, DOI: 10.1166/Sl.2011.1435.

[105] S. H. Choi, G. Ankonina, D. Y. Youn, S. G. Oh, J. M. Hong, A. Rothschild and I. D. Kim, *ACS Nano*, 2009, **3**, 2623–2631, DOI: 10.1021/nn900126k.

[106] M. Ahmad, C. F. Pan, Z. X. Luo and J. Zhu, *Journal of Physical Chemistry C*, 2010, **114**, 9308–9313, DOI: 10.1021/jp102505g.

[107] L. Liu, S. Li, J. Zhuang, L. Wang, J. Zhang, H. Li, Z. Liu, Y. Han, X. Jiang and P. Zhang, *Sensors and Actuators B: Chemical*, 2011, **155**, 782–788, DOI: 10.1016/j.snb.2011.01.047.

[108] L. Wang, S. Wang, M. Xu, X. Hu, H. Zhang, Y. Wang and W. Huang, *Physical Chemistry Chemical Physics*, 2013, **15**, 17179–17186, DOI: 10.1039/c3cp52392f.

[109] Y. Zheng, L. Zheng, Y. Zhan, X. Lin, Q. Zheng and K. Wei, *Inorganic Chemistry*, 2007, **46**, 6980–6986, DOI: 10.1021/ic700688f.

[110] N. Tamaekong, C. Liewhiran, A. Wisitsoraat and S. Phanichphant, *Sensors*, 2009, **9**, 6652–69, DOI: 10.3390/s90906652.

[111] S. M. Wang, P. Wang, Z. F. Li, C. H. Xiao, B. X. Xiao, R. Zhao, T. Y. Yang and M. Z. Zhang, *RSC Advances*, 2014, **4**, 35375–35382, DOI: 10.1039/C4ra05462h.

[112] Z. Ling, C. Leach and R. Freer, *Journal of the European Ceramic Society*, 2001, **21**, 1977–1980, DOI: 10.1016/S0955-2219(01)00154-6.

[113] Y. Hu, X. Zhou, Q. Han, Q. Cao and Y. Huang, *Materials Science and Engineering: B*, 2003, **99**, 41–43, DOI: 10.1016/S0921-5107(02)00446-4.

[114] G. Lu, S. Park, K. Yu, R. S. Ruoff, L. E. Ocola, D. Rosenmann and J. Chen, *ACS Nano*, 2011, **5**, 1154–64, DOI: 10.1021/nn102803q.

[115] L. H. Tang, Y. Wang, Y. M. Li, H. B. Feng, J. Lu and J. H. Li, *Advanced Functional Materials*, 2009, **19**, 2782–2789, DOI: 10.1002/adfm.200900377.

[116] E. Llobet, *Sensors and Actuators B: Chemical*, 2013, **179**, 32–45, DOI: 10.1016/j.snb.2012.11.014.

[117] W. J. Yuan and G. Q. Shi, *Journal of Materials Chemistry A*, 2013, **1**, 10078–10091, DOI: 10.1039/c3ta11774j.

[118] A. S. M. I. Uddin and G. S. Chung, *Sensors and Actuators B: Chemical*, 2014, **205**, 338–344, DOI: 10.1016/j.snb.2014.09.005.

[119] A. Katoch, G. J. Sun, S. W. Choi, J. H. Byun and S. S. Kim, *Sensors and Actuators B: Chemical*, 2013, **185**, 411–416, DOI: 10.1016/j.snb.2013.05.030.

[120] S. Stankovich, D. A. Dikin, R. D. Piner, K. A. Kohlhaas, A. Kleinhammes, Y. Jia, Y. Wu, S. T. Nguyen and R. S. Ruoff, *Carbon*, 2007, **45**, 1558–1565, DOI: 10.1016/j.carbon.2007.02.034.

[121] P. Cui, J. Lee, E. Hwang and H. Lee, *Chemical Communications*, 2011, **47**, 12370–2, DOI: 10.1039/c1cc15569e.

[122] H. W. Kim, M. A. Kebede, H. S. Kim, B. Srinivasa, D. Y. Kim, J. Y. Park and S. S. Kim, *Current Applied Physics*, 2010, **10**, 52–56, DOI: 10.1016/j.cap.2009.04.010.

[123] J. Zhang, H. Yang, G. Shen, P. Cheng, J. Zhang and S. Guo, *Chemical Communications*, 2010, **46**, 1112–1114, DOI: 10.1039/b917705a.

[124] N. Barsan and U. Weimar, *Journal of Electroceramics*, 2001, **7**, 143–167, DOI: 10.1023/A:1014405811371.

[125] S. S. Kim, J. Y. Park, S. W. Choi, H. G. Na, J. C. Yang and H. W. Kim, *Journal of Alloys and Compounds*, 2011, **509**, 9171–9177, DOI: 10.1016/j.jallcom.2011.06.104.

[126] K. Anand, O. Singh, M. P. Singh, J. Kaur and R. C. Singh, *Sensors and Actuators B: Chemical*, 2014, **195**, 409–415, DOI: 10.1016/j.snb.2014.01.029.

[127] R. J. Zou, G. J. He, K. B. Xu, Q. Liu, Z. Y. Zhang and J. Q. Hu, *Journal of Materials Chemistry A*, 2013, **1**, 8445–8452, DOI: 10.1039/c3ta11490b.

[128] A. Bagri, C. Mattevi, M. Acik, Y. J. Chabal, M. Chhowalla and V. B. Shenoy, *Nature Chemistry*, 2010, **2**, 581–7, DOI: 10.1038/nchem.686.

[129] Z. Y. Zhang, R. J. Zou, G. S. Song, L. Yu, Z. G. Chen and J. Q. Hu, *Journal of Materials Chemistry*, 2011, **21**, 17360–17365, DOI: 10.1039/c1jm12987b.

[130] T. Hubert, L. Boon-Brett, V. Palmisano and M. A. Bader, *International Journal of Hydrogen Energy*, 2014, **39**, 20474–20483, DOI: 10.1016/j.ijhydene.2014.05.042.

[131] W. J. Buttner, M. B. Post, R. Burgess and C. Rivkin, *International Journal of Hydrogen Energy*, 2011, **36**, 2462–2470, DOI: 10.1016/j.ijhydene.2010.04.176.

[132] C. S. Hsu, H. I. Chen, P. C. Chou, J. K. Liou, C. C. Chen, C. F. Chang and W. C. Liu, *IEEE Sensors Journal*, 2013, **13**, 1787–1793, DOI: 10.1109/Jsen.2013.2243430.

[133] T. Hubert, L. Boon-Brett, G. Black and U. Banach, *Sensors and Actuators B: Chemical*, 2011, **157**, 329–352, DOI: 10.1016/j.snb.2011.04.070.

[134] E. Comini and G. Sberveglieri, *Materials Today*, 2010, **13**, 28–36, DOI: 10.1016/S1369-7021(10)70126-7.

[135] W. Wang, H. M. Huang, Z. Y. Li, H. N. Zhang, Y. Wang, W. Zheng and C. Wang, *Journal of the American Ceramic Society*, 2008, **91**, 3817–3819, DOI: 10.1111/j.1551-2916.2008.02765.x.

[136] Y. B. Zhang, J. Yin, L. Li, L. X. Zhang and L. J. Bie, *Sensors and Actuators B: Chemical*, 2014, **202**, 500–507, DOI: 10.1016/j.snb.2014.05.111.

[137] A. Katoch, S. W. Choi, H. W. Kim and S. S. Kim, *Journal of Hazardous Materials*, 2015, **286**, 229–35, DOI: 10.1016/j.jhazmat.2014.12.007.

[138] R. Eischens, *Journal of Catalysis*, 1962, **1**, 180–191, DOI: 10.1016/0021-9517(62)90022-2.

[139] W. Kim, G. Kwak, M. Jung, S. K. Jo, J. B. Miller, A. J. Gellman and K. Yong, *Journal of Physical Chemistry C*, 2012, **116**, 16093–16097, DOI: 10.1021/Jp304191m.

[140] F. Vines, A. Iglesias-Juez, F. Illas and M. Fernandez-Garcia, *Journal of Physical Chemistry C*, 2014, **118**, 1492–1505, DOI: 10.1021/jp407021v.

[141] D. G. Thomas and J. J. Lander, *The Journal of Chemical Physics*, 1956, **25**, 1136, DOI: 10.1063/1.1743165.

[142] C. W. Na, H. S. Woo, I. D. Kim and J. H. Lee, *Chemical Communications*, 2011, **47**, 5148–5150, DOI: 10.1039/c0cc05256f.

[143] S. Deng, V. Tjoa, H. M. Fan, H. R. Tan, D. C. Sayle, M. Olivo, S. Mhaisalkar, J. Wei and C. H. Sow, *Journal of the American Chemical Society*, 2012, **134**, 4905–4917, DOI: 10.1021/ja211683m.

[144] G. Neri, S. G. Leonardi, M. Latino, N. Donato, S. Baek, D. E. Conte, P. A. Russo and N. Pinna, *Sensors and Actuators B: Chemical*, 2013, **179**, 61–68, DOI: 10.1016/j.snb.2012.10.031.

[145] L. A. Patil, M. D. Shinde, A. R. Bari and V. V. Deo, *Sensors and Actuators B: Chemical*, 2009, **143**, 270–277, DOI: 10.1016/j.snb.2009.09.048.

[146] N. S. Baik, G. Sakai, N. Miura and N. Yamazoe, *Sensors and Actuators B: Chemical*, 2000, **63**, 74–79, DOI: 10.1016/S0925-4005(99)00513-4.

[147] K. Yao, W. W. Gong, Y. F. Hu, X. L. Liang, Q. Chen and L. M. Peng, *Journal of physical chemistry C*, 2008, **112**, 8721–8724, DOI: 10.1021/jp8022293.

[148] B. Wang, L. F. Zhu, Y. H. Yang, N. S. Xu and G. W. Yang, *Journal of Physical Chemistry C*, 2008, **112**, 6643–6647, DOI: 10.1021/Jp8003147.

VITA

The author received his B.S (Engineering) in Materials Science and Engineering from, one of the most prestigious institutes of Pakistan, Ghulam Ishaq Khan Institute of Engineering Sciences and Technology (GIK Institute), in June 2014. He won the merit based "Government of Punjab" scholarship among ten other students from Punjab province (the most populous province of Pakistan). His Final year project during undergraduate studies was "Optimization of Mechanical Properties of NiTi Shape Memory Alloys for Biomedical Applications". In this project, he applied Finite Element Analysis (FEA) techniques using ANSYS (a commercial FEA package) to optimize the mechanical properties (such as compressive strength, stiffness *etc,*) of NiTi shape memory alloys, in order to enhance their quality for biomedical applications.

Soon after his graduation, he joined Nano Thin Film Lab at Inha University, Republic of Korea for Masters in Engineering under the supervision of Professor Sang Sub Kim. During his masters program, he was awarded full Inha University's prestigious international scholarship (Jungseok International Scholarship). His research was focused on the synthesis of composite nanomaterials (especially composites of metal oxide based materials with graphene and reduced graphene oxide) and their applications in chemical gas sensors to enhance the quality of safety, environmental monitoring and for noninvasive medical diagnostics such as sensors for breath analysis.

Furthermore, he is also interested in some other applications of advanced nanomaterials especially in the areas of energy production and storage, biomaterials for smart drug delivery, and physics and science of nanomaterials.